





Article

Micro-Computed Tomography Soft Tissue Biological Specimens Image Data Visualization

Branislav Gaspar ¹, Jana Mrzilkova ², Jiri Hozman ¹, Petr Zach ^{2,*}, Anastasiya Lahutsina ², Alexandra Morozova ², Giulia Guarnieri ³ and Jitka Riedlova ²

¹ Department of Biomedical Technology, Faculty of Biomedical Engineering, Czech Technical University in Prague, Nam. Sitna 3105, 272 01 Kladno, Czech Republic; gaspabra@student.cvut.cz (B.G.); hozman@fbmi.cvut.cz (J.H.)

² Department of Anatomy, Third Faculty of Medicine, Charles University, Ruska 87, 100 00 Prague, Czech Republic; mrzilkova.jana@seznam.cz (J.M.); anastasiya.lahutsina@lf3.cuni.cz (A.L.); alexandra.morozova@lf3.cuni.cz (A.M.); jitka.riedlova@lf3.cuni.cz (J.R.)

³ Department of Experimental and Clinical Medicine, Anatomy and Histology Section, University of Firenze, Largo Brambilla 3, 50134 Firenze, Italy; giulia.guarnieri@unifi.it

* Correspondence: zach.petr@post.cz

Abstract: Visualization of soft tissues in microCT scanning using X-rays is still a complicated matter. There is no simple tool or methodology on how to set up an optimal look-up-table while respecting the type of soft tissue. A partial solution may be the use of a contrast agent. However, this must be accompanied by an appropriate look-up-table setting that respects the relationship between the soft tissue type and the Hounsfield units. The main aim of the study is to determine experimentally derived look-up-tables and relevant values of the Hounsfield units based on the statistical correlation analysis. These values were obtained from the liver and kidneys of 24 mice in solutions of ethanol as the centroid value of the opacity look-up-table area under this graph. Samples and phantom were scanned by a Bruker SkyScan 1275 micro-CT and Phywe XR 4.0 and processed using CTvox and ORS Dragonfly software. To reconstruct the micro-CT projections, NRecon software was used. The main finding of the study is that there is a statistically significant relationship between the centroid of the area under the look-up-table curve and the number of days for which the animal sample was stored in an ethanol solution. H1 of the first hypothesis, i.e. that suggested the Spearman's correlation coefficient does not equal zero ($r_1 \neq 0$) regarding this relationship was confirmed. On the other hand, there is no statistically significant relationship between the centroid of the area under the look-up-table curve and the concentration of the ethanol solution. In this case, H1 of the second hypothesis, i.e. that the Spearman's correlation coefficient does not equal zero ($r_2 \neq 0$) regarding this relationship was not confirmed. Spearman's correlation coefficients were -0.27 for the concentration and -0.87 for the number of days stored in ethanol solution in the case of the livers of 13 mice and 0.06 for the concentration and 0.94 for the number of days stored in ethanol solution in the case of kidneys of 11 mice.

Keywords: micro-CT; transfer function; look-up-table; soft tissue; CT number; Hounsfield unit; visualization



Citation: Gaspar, B.; Mrzilkova, J.; Hozman, J.; Zach, P.; Lahutsina, A.; Morozova, A.; Guarnieri, G.; Riedlova, J. Micro-Computed Tomography Soft Tissue Biological Specimens Image Data Visualization. *Appl. Sci.* **2022**, *12*, 4918. <https://doi.org/10.3390/app12104918>

Academic Editors: Cecilia Di Ruberto, Andrea Loddo, Lorenzo Putzu, Alessandro Stefano and Albert Comelli

Received: 25 February 2022

Accepted: 11 May 2022

Published: 12 May 2022

Publisher's Note: MDPI stays neutral with regard to jurisdictional claims in published maps and institutional affiliations.



Copyright: © 2022 by the authors. Licensee MDPI, Basel, Switzerland. This article is an open access article distributed under the terms and conditions of the Creative Commons Attribution (CC BY) license (<https://creativecommons.org/licenses/by/4.0/>).

1. Introduction

Computed tomography (CT) imaging is widely used in medical practice, mainly due to the non-invasiveness of this method, its good spatial resolution, and the relatively short acquisition time of the required images. In addition to conventional CT, which is mainly used both for diagnostic and therapeutic procedures [1], high spatial resolution CT or micro-CT (μ CT) are also used in practice [2]. These systems work on the same basic principle as the typical CT, except that the X-ray-tube-detector system does not perform rotational motion, but rotates the specimen. However, their advantage lies in their ability to scan samples with much higher spatial ($<50 \mu\text{m}$) and contrast resolution.

It is because of the non-destructiveness of this method in evaluating the scanned volume with high resolution that μ CT devices are much used in both research and industry. Furthermore, even if the intrinsic noise of commercial μ CT detectors is not a problem in many cases (especially in industry), the imaging of more delicate structures with a lower range of CT numbers (the same as Hounsfield units = HU), and the associated lower attenuation contrast between structures, such as soft tissues, is greatly hampered by this noise.

The present work, in collaboration with the Department of Anatomy at the 3rd Faculty of Medicine, Charles University (Prague, Czech Republic), is primarily focused on the visualization of soft tissues in particular, as well as the search for a methodology that could optimize the overall visualization process and make it easier. This also involves research and experimentation with new procedures and contrast agents to achieve the required contrast between soft tissues that is needed for visualization [3–7].

Two papers dealt with similar issues. The first one, i.e., [8], used an image histogram for optimal look-up-table (LUT) setup. Thus, it is not the same intention. The second work, i.e., [9], uses only the LUT settings. However, in neither case was it possible to find a link between soft tissue type and Hounsfield units.

We have been using μ CT for a long time and we need to visualize soft tissues in experimental animals. For a long time, there is a tradition of contrast agent usage, but they are not always best and/or we often encounter problems when using them. This is why we tried to figure out some connection between LUT setting and HU values for individual structures and organs; even mentioned contrast agents could have been of some value in this. Additionally, we wanted to find out if there exist other possibilities of contrast enhancement, e.g., because of air bubbles in contrast agent for ultrasound. Especially this is considered when experimenting with PHYWE XR 4.0 in various structures in chicken tissues (phantom). Finally, we also think about semiautomated, or fully automated settings of LUT with fuzzy logic. Some of these ideas were verified within this study.

The main aim of this study is to optimize soft tissue contrast visualization of biological specimens (mouse liver, kidneys) using a contrast agent and a proper LUT. Based on this aim we would like to statistically verify the relationship between the centroid of the area under the look-up-table curve and the number of days for which the animal sample was stored in the ethanol solution, as well as the concentration of the ethanol solution. Therefore, two hypotheses were formulated. H1 (Each occurrence of H1 means that it is an alternative hypothesis) of the first hypothesis states that the Spearman's correlation coefficient does not equal zero ($r_1 \neq 0$) in the case of relationship between the coordinates of the center of gravity (centroid) of the area under the LUT and the number of days for which the sample was stored in the ethanol solution. H1 of the second hypothesis states that the Spearman's correlation coefficient does not equal zero ($r_2 \neq 0$) in the case of relationship between the coordinates of the center of gravity (centroid) of the area under the LUT and the ethanol concentration in the solution.

2. Materials and Methods

2.1. Materials, Devices, and Software

The database of μ CT images from the Dept. of Anatomy of the 3rd Medical Faculty of Charles University was used for the study.

All intravenous contrast agent's applications follow similar pattern. At first there is introduced the contrast agent into the tail vein. After that follows animal euthanasia and μ CT scanning. Concerning Aurovist contrast agent, solution from the ampoule is injected into tail vein under isoflurane anesthesia into the bloodstream. Follows scanning in the μ CT apparatus. Concerning the timing, scanning is performed after complete distribution of Aurovist gold nanoparticles to the tissues of the animal, including both arteries and veins of the circulatory system.

Preparation steps for experimental animals were the following.

Animals (mice) were housed in the standard light/dark cycle in the First Faculty of Medicine, Charles University at standard room temperature. Mice were applied one ampulla of Aurovist contrast agent (15 nm of Aurum particles in 40 mg of solution, Nanoprobe, Yaphank, NY, USA) in the tail vein per one mouse. In case of whole mouse experiment, 2 h after Aurovist application were mice euthanized with pentobarbital and scanned in micro-CT. Timing was selected because rigor mortis develops within 2 h after death.

Animals (chickens) were obtained by micro-surgery from the eggs in their 19 days of development. Firstly, a rectangular window was dissected out of the egg wall and solution of 40% KI to euthanize chicken (heartbeat stop) was applied intra-amniotically. After the removal of dead chicken from the egg it was placed into 80% of Ethanol for 7 days.

Animals (rabbits) were donated by Prof. Berndt Minnich, University of Salzburg, Vascular Unit, Austria. Post-mortem, rabbits were pinned in supine position onto a wax plate. After opening of the abdomen, the aorta abdominalis was identified and separated from each other. A ligature around the aorta abdominalis ensured exclusive upper body casting. A tube was inserted into the artery cranially to the first ligature and tied in place (6.0 sutures). Blood vessels were rinsed after opening the aorta with 0.9% Ringer's solution (60 mL/h) at 37 °C until clear reflux appeared. Thereafter, the casting medium (Mercor-CL-2B, Ladd Research Inc., Burlington, VT, USA) diluted with monomeric methyl methacrylate was injected at 99 mL/h by an electric syringe pump (Habel PSA 50, Sky Electronics S.A., Grenoble, France) or a pneumatic injection pump (ComServ OG, Ebenau, Austria). When the injected resin became viscous, animals were left in place for at least 30 min at room temperature (RT) to initiate resin polymerization. The upper bodies of the rabbits were cut off and tempered in water (60 °C, 24 h). Subsequently, water was replaced by potassium hydroxide (7.5%, 40 °C, twice for 24 h), followed by hydrochloric acid (2%, RT, 24 h) and formic acid (5%, RT, 15 min). Finally, casts were washed thrice and frozen in distilled water (−20 °C) and freeze-dried (FreeZone 77520, Labconco Corp., Kansas City, MO, USA).

The database consisted of ex vivo chickens in and out of the shell and aged 5 to 19 days. Chickens outside the shell were preserved in 50–100% ethanol solution, some of them additionally in formaldehyde solution. In addition, a few chicken samples contained injected gold nanoparticles from the Aurovist contrast agent. Prior to acquisition, samples were left in air after removal from the solution and scanned with Bruker's SkyScan 1275 (Bruker MicroCT, Kontich, Belgium) after evaporation of the solution.

Another part of the database consisted of ex vivo preparations of mice injected with Aurovist contrast agent containing 15 nm gold nanoparticles (AuNPs) prior to scanning.

A 50% solution of Omnipaque contrast agent was then used intravenously before scanning the mouse organs themselves (liver, lungs, spleen, and heart).

Some mouse organs, such as liver, kidney, brain, heart, and leg, were kept for one week in a solution of potassium iodide with concentration 100 mM (KI, Merck, Czech Republic) in 20% ethanol before scanning.

Lastly, the database included corrosive preparations in which a resin (Mercor) [10] was infused into the vascular system and allowed to harden, the remaining tissue was then dissolved in lye by maceration and the sample was scanned. Corrosive preparations of rabbit and rat lung and heart were selected for the purpose of this study.

For the implementation of the idea of blood vessels visualization in soft tissue using the contrast that would be created by the presence of air in the vascular cavities, chicken flesh was used as a phantom in which cylindrical tubes/capillaries of various diameters made of different materials were placed. These were two tubes (silicone), a glass capillary with sealed ends, and a plastic straw (bioplastic PLA). This phantom, depicted in Figure 1, was then scanned with the Phywe XR 4.0 (PHYWE Systeme GmbH & Co. KG, Göttingen, Germany) experimental setup.

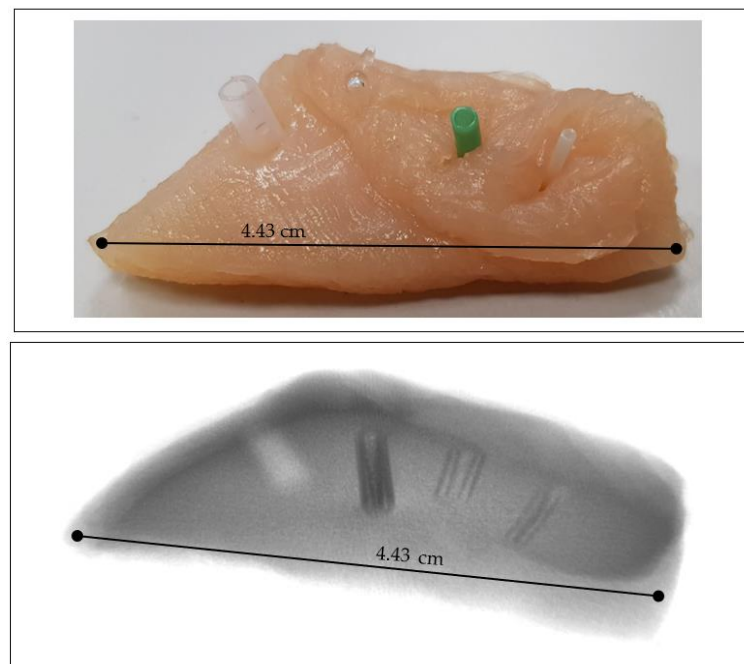


Figure 1. Chicken sample with capillaries as vascular phantom (top) and phantom X-ray image (bottom); materials from left: bioplastic PLA, glass, green silicone, and transparent silicone. Scale is in [cm].

Two μ CT systems were used to scan the above samples. The ex vivo chicken samples were scanned with a professional μ CT system Bruker SkyScan 1275 located at the Department of Anatomy, 3rd Faculty of Medicine, Charles University, while the Phywe XR 4.0 experimental setup was used to scan the phantom of the chicken vasculature and capillaries at the Dept. of Biomedical Technology, Fac. of Biomedical Engineering, Czech Technical University in Prague.

Bruker's SkyScan 1275 has been specifically designed for fast scanning using advances in X-ray source technology and efficient flat-panel detectors. This X-ray source has the selectable anode voltage of the assembly ranging from 20 to 100 kV and the max. available power is 10 W. The assembly includes an active 3 megapixel CMOS flat-panel detector with a maximum possible resolution of up to 4 μ m (at maximum magnification) and it is capable of accommodating a sample diameter of 96 mm and a height of 120 mm. All used setups of the above mentioned μ CT are available within the Appendix B, i.e., Tables A2–A19.

The XR 4.0 experimental setup from the German company Phywe was designed for teaching purposes and for laboratory experiments with X-rays. Its advantage lies, among other things, in the relatively easy and quick interchangeability of the X-ray tube and, therefore, facilitates experiments with different anode materials [11,12].

The XR 4.0 can also be used as a μ CT system thanks to an expansion kit supporting the computed tomography function. This set consists of a fixed copper X-ray tube that illuminates the specimen on a rotary table driven by a stepper motor with a minimum adjustable table rotation angle of 0.086°. The attenuated X-ray radiation is then incident on an XRIS detector (CMOS) with an active area of 5 \times 5 cm² and a maximum possible resolution of 48 μ m [11,12]. The selectable anode voltage of the assembly is 5–35 kV with an adjustable emission current in the range up to 1 mA. Setup with detailed setting is available within the Appendix B, i.e., Table A1.

As regards the software, CTvox (Version 3.3.1, 3D.SUITE Software, Bruker MicroCT, Kontich, Belgium) [13] and ORS Dragonfly (Version 2020.2 Build 941, Montreal, QC, Canada) [14] software were used for suitable visualization. Within an additional part of the study there were used NRecon (Version 1.7.4.2, Bruker MicroCT, Kontich, Belgium) [15] and Measure CT (Version 2.0, PHYWE Systeme GmbH & Co. KG, Göttingen, Germany) [12]

software to reconstruct the μ CT projections. Software MIPS (Version 2.0, Czech Technical University in Prague, Faculty of Biomedical Engineering, Kladno, Czech Republic) [16] was used for illustration purposes only.

2.2. Methods

In the field of digital image data processing (digital images), various point operators or functions are very often used to perform single-point assignment, or transform the value of an image point (pixel) from an input image (labeled a) at a given position (x, y) to another value within the output image (labeled b), but at the same position (x, y). In general, this situation is indicated in Figure 2.

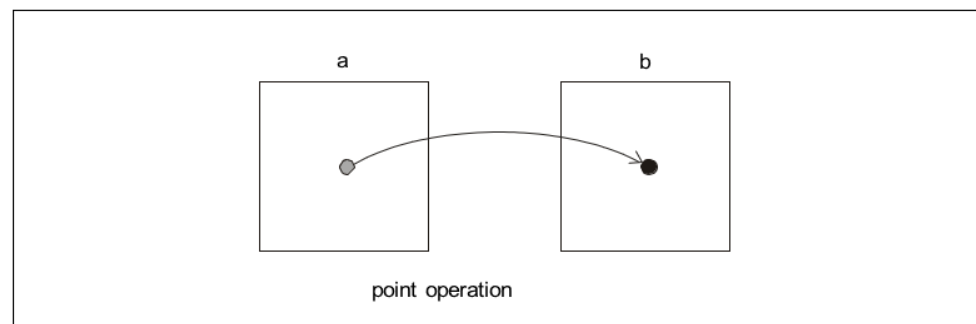


Figure 2. Diagram of general principle of the point operator (function)—the output of which is an unambiguous assignment of the value of a pixel in the output image. It is related to the value of a pixel in the input image.

2.2.1. Transfer Functions, Resp. Look-up-Table Concept

Let us consider an experiment where we multiply the pixel values in the input image by 1. If we consider the usual input dynamic range of grayscale digital images (i.e., 0 to 255, where 0 represents the black level and 255 represents the white level), then the output image will produce a result that is identical to the values in the input image. For example, an input value of 10 would be multiplied by 1 and the result would also be 10 and this would continue for all pixel values in all positions. This then results in a simple linear function that can be represented as a straight line at a 45° angle and passing through the origin of the coordinates, or it is a simple copy of the input image. Such an example can also be expressed very simply in mathematical notation, namely the slope equation of the straight line as reported in Figure 3.

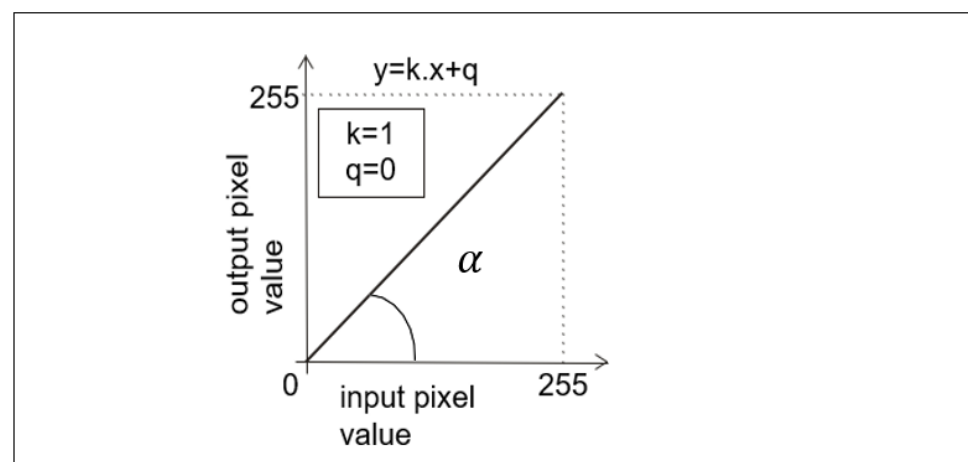


Figure 3. Example of a point operator (function) that implements a copy of the input image on the output. In this case, the value of the slope (i.e., $k = 1$), and the value of the y-intercept of a straight line where a line crosses y-axis of a graph (i.e., $q = 0$).

With this defined operator, we can easily adjust various changes to image parameters such as brightness and contrast, both when we need to highlight selected gray levels or when we need to suppress them. Examples of different transfer functions are shown in Figures 4 and 5.

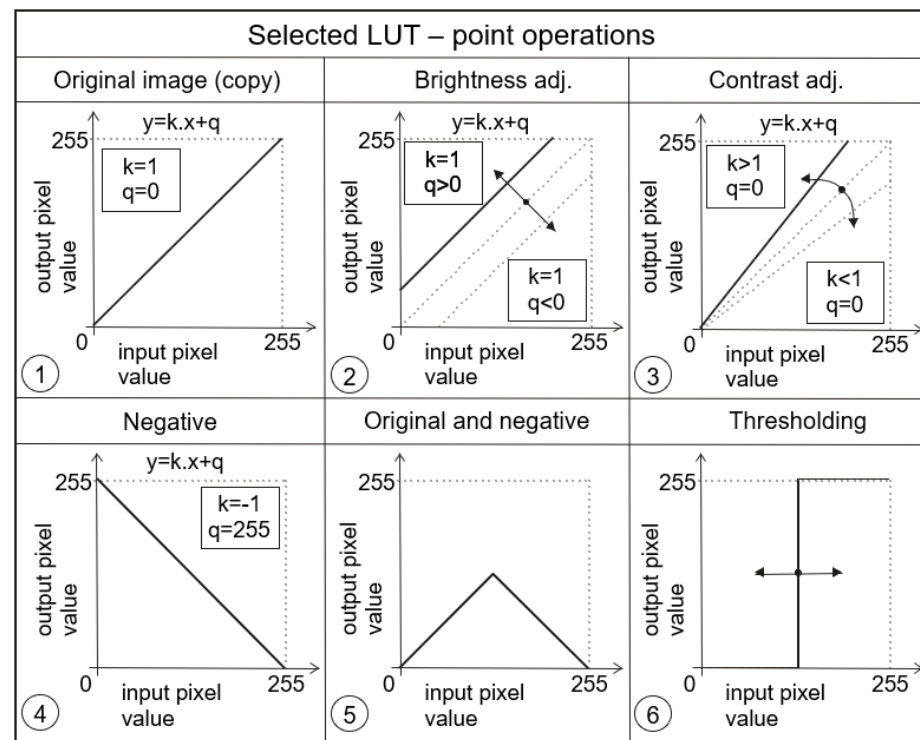


Figure 4. Examples of different point operators (functions) being very often used.

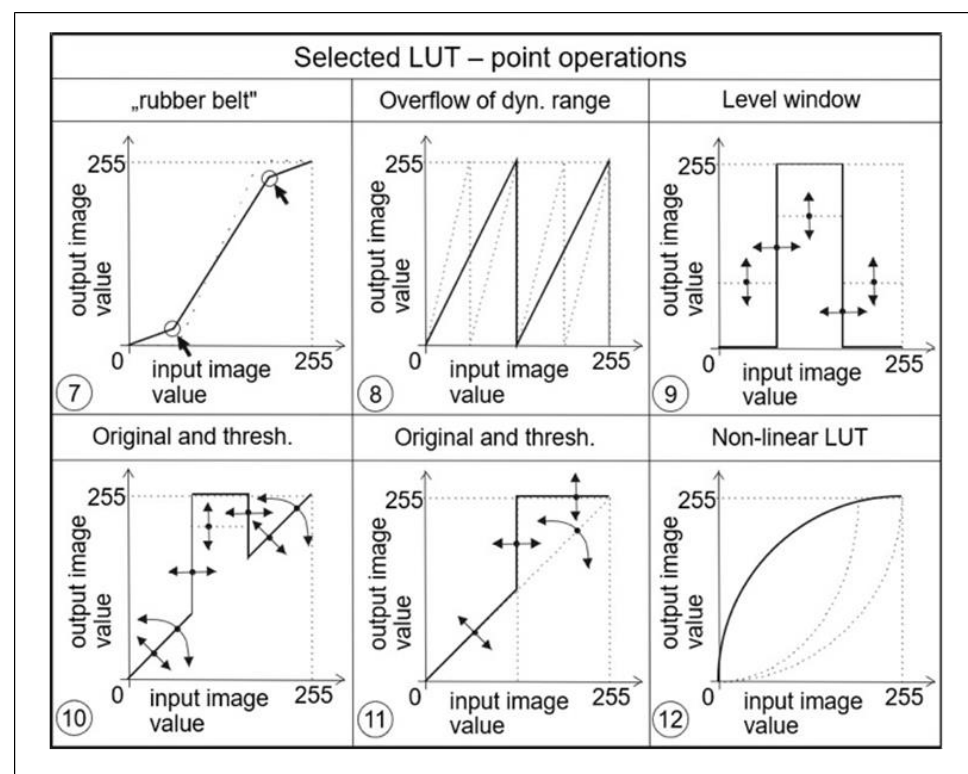


Figure 5. Examples of other point operators (functions) that could also be utilized.

From the above examples, it is clear that these transfer functions or LUTs allow to significantly influence the visualization process of the given image data. Thus, for example, the transfer function in Figure 4 (panel 2) affects the brightness of the image, in Figure 4 (panel 3) it affects the contrast, in Figure 4 (panel 6) a transfer function for realizing a so-called binary image (i.e., an image that contains only two levels, most often black and white) is shown, and yet another suitable example can be seen in Figure 5 (panel 12), which is suitable for correcting an image that was taken under greatly reduced or increased lighting conditions. The latter two examples are further illustrated in the image data, respectively, in Figures 6 and 7.

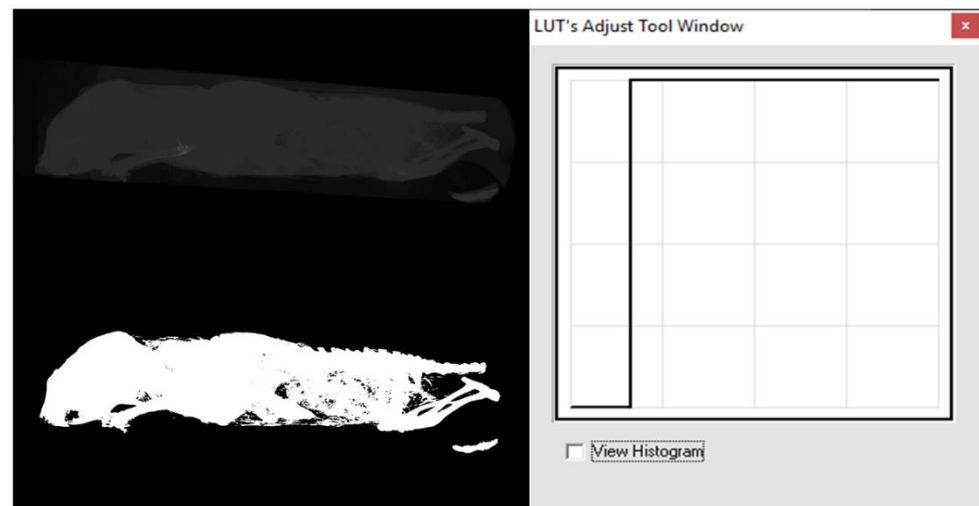


Figure 6. Example of a point operator (function)—thresholding or binarization [16].

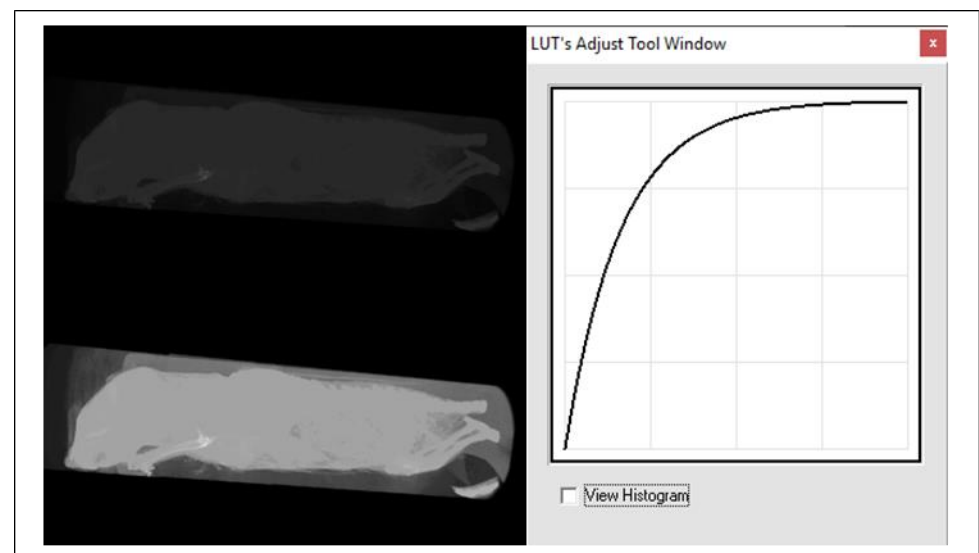


Figure 7. Examples of point operator (function)—logarithmic function [16].

2.2.2. Transfer Functions Related to the Hounsfield Units (HU)

There is a very important process in CT and μ CT imaging, that is the actual conversion of the attenuation of the passing X-rays to the grey level. Based on the physiological properties of human vision, 256 gray levels are very often used. The range of so-called Hounsfield units (HU) is typically in the range -1024 to $+3071$, which is 4096 values, and this is a much larger dynamic range than the 256 gray level values. For this reason, only the so-called windows on a given tissue (limited HU range), which has a width of 256 values or greater, need to be displayed. Thus, it is never possible to see all tissues at once, see

soft tissue window, bone window, etc. Realistically, this situation is often implemented by a transfer function that has HU values on the x -axis and gray level values from 0 to 255 on the vertical axis. The situation is also depicted in Figure 8, which is an example of this situation in NRecon software [15].

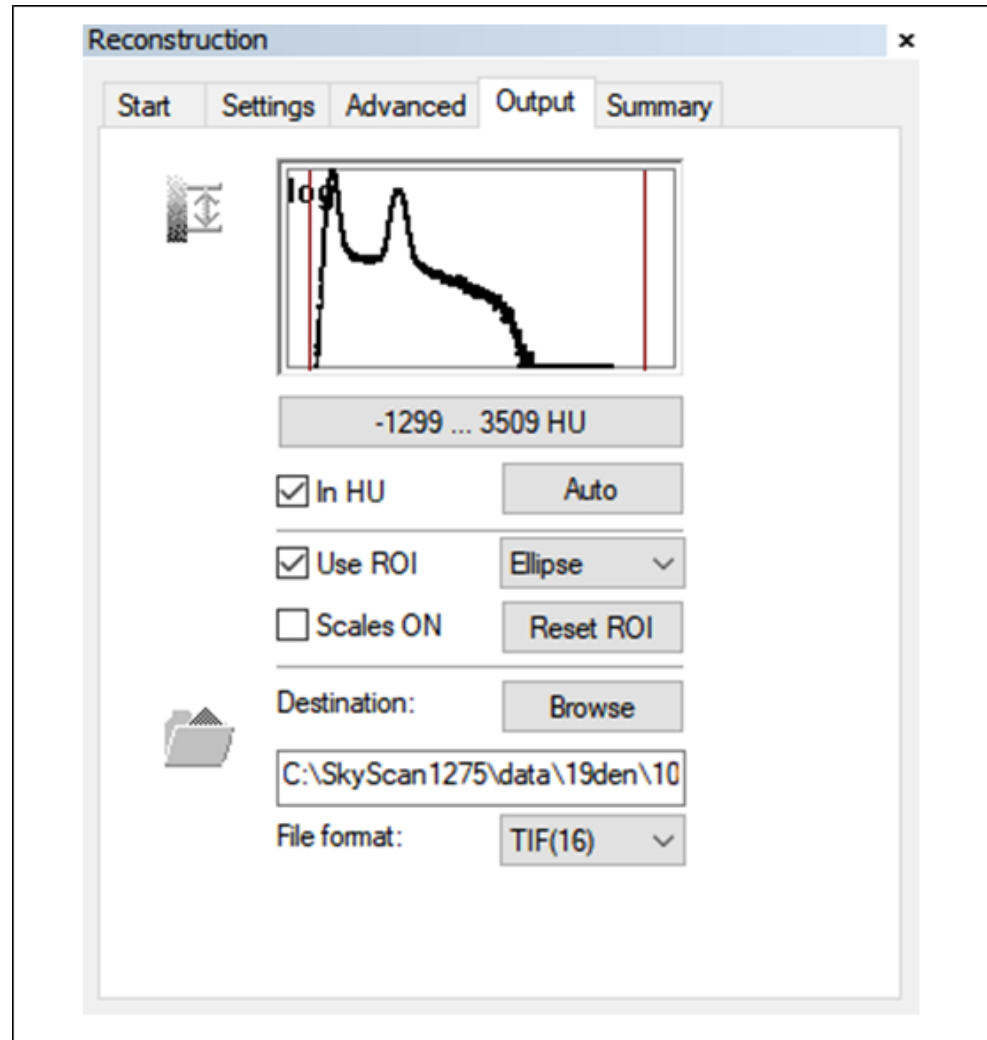


Figure 8. Nrecon SW MENU detail—reconstruction of outputs (parameter settings).

The practical impact of this situation is also the arrangement of the image data format in the form of so-called DICOM (Digital Imaging and Communications in Medicine) files. This file contains both image data and metadata [17] and each DICOM browser can display both. The structure of DICOM files consists of so-called tags and an example of these tags in relation to HU are the following items (i.e., the DICOM attribute number (0028,1053) whose name is “Rescale slope” and the DICOM attribute number (0028,1052) whose name is “Rescale intercept”). These parameters can then be substituted into the equation after the parameters k and q in Figure 3. These items can also be read.

2.2.3. Transfer Functions Design Possibilities

Within the Ctvox software a histogram of the attenuation is available together with an editor that can be used to freely modify the transfer functions as LUTs, i.e., the program can either simply connect individual markers or use them as nodes to create a so-called spline curve. The program then assigns to each voxel the corresponding degree of the currently selected parameter (the so-called emission color [18]) depending on the attenuation of the voxel in the spline mode called volume rendering.

There are five parameters to choose from—opacity, red (R) channel, green (G) channel, blue (B) channel, and luminance (L), as reported in Figure 9c. If all three RGB channels are combined, only two parameters are available (i.e., opacity and luminance), and the voxels are assigned to their opacity and grayscale. In the other case, four parameters are available, namely, opacity together with all three RGB channels. In addition to assigning opacities, individual voxels can also be colored differently in this way, or segmented by color. In the case of opacity, there is available a purple opacity curve (initially a straight line, with just two markers) appears, in order to indicate that it is active. Opacity is the opposite of transparency. Hence, we will need to map low intensities to low opacities (i.e., high transparency), as shown in Figure 9c.

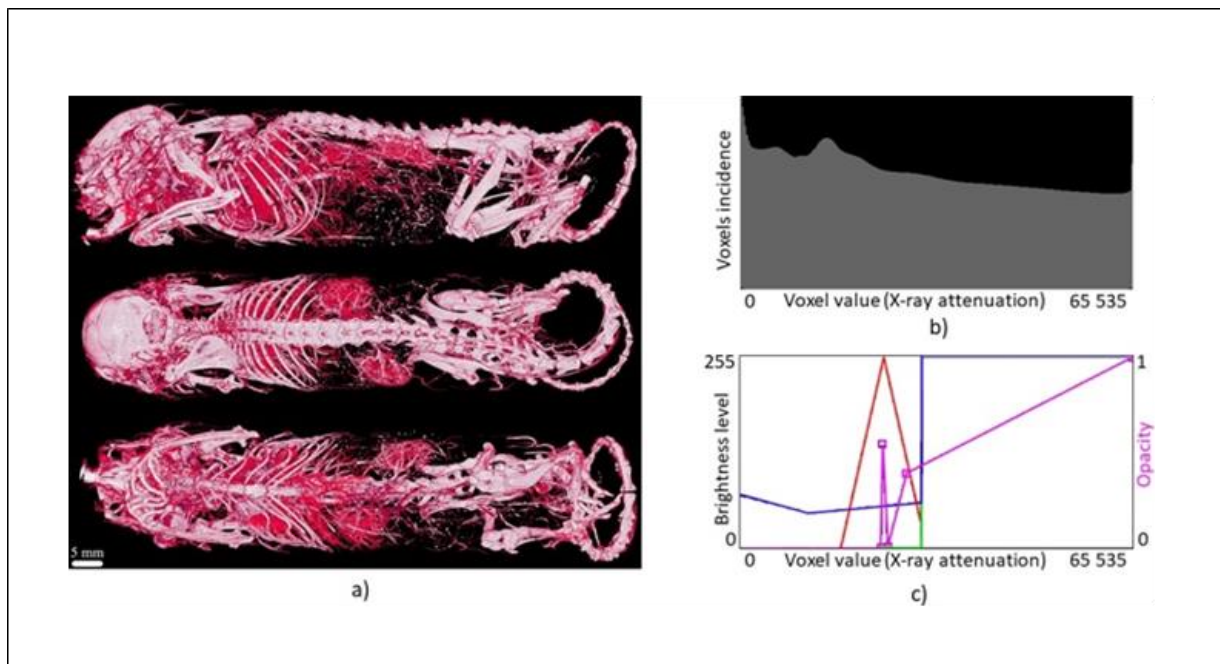


Figure 9. Transfer functions design—(a) mouse (Aurovist, 42 kV), (b) histogram, and (c) transfer functions (opacity, RGB).

3. Results

A total of 53 transfer functions (LUTs) were designed, 42 of which were validated and optimized to emphasize the soft tissues of selected biological samples from μ CT (mouse, rat, rabbit) using selected contrast agents (Aurovist, Omnipaque, KI in the ethanol solution, Mercor). The remaining 11 transfer functions could not be verified due to the absence of contrast in soft tissue samples from chickens. In total, 18 images and transfer functions are included within this text.

Out of the 53 transfer functions, one transfer function was able to be suggested that would likely highlight the tongue of a 19-day-old chick scanned with the Bruker SkyScan 1275 [19] at an anode voltage of 40 kV.

A total of 24 mice samples were statistically processed via correlation. Normality test was performed for all these samples in Matlab (Campus Wide Matlab, R2021a, The MathWorks, Inc., Natick, MA, USA) via Lilliefors test. These values were obtained for liver and kidneys of 24 mice in solutions of ethanol as a centroid value of the opacity LUT area under this graph (see example on Figure 10). Except for one dataset, all the others do not have a normal distribution according to this test. Results are available within Tables 1–4 below. From this follows that there is required to use Spearman's correlation coefficient.

In Figure 10, we can see example of the opacity LUT with marked points, i.e., $[X_1, Y_1]$, $[X_2, Y_2]$, and $[X_3, Y_3]$ whereby coordinate $Y_1 = 0$ and $Y_3 = 0$. These points form a homogeneous triangle that enables simplified computation of the centroid.

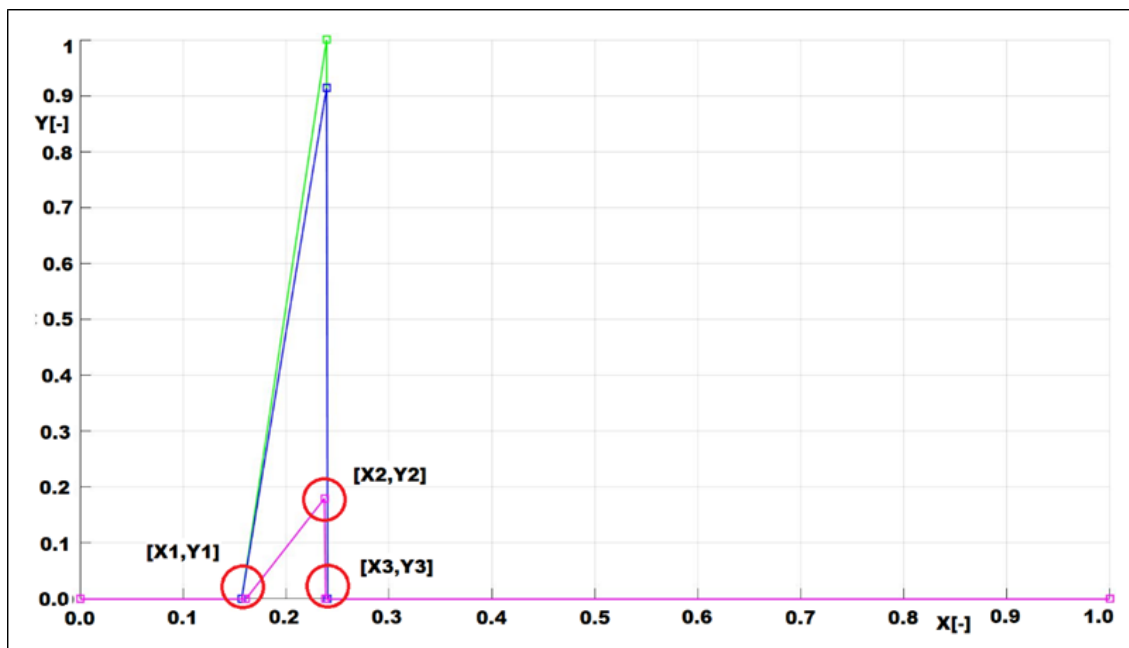


Figure 10. Example of the opacity (pink color) LUT with marked points that are used for computation of the centroid. Such figure exists for every included image (mouse_1_liver_ethanol_100_%_day_16).

Table 1. *p*-values of the Lilliefors test of normality.

Parameter	Value <i>p</i> -Value	Note
X' — <i>x</i> coordinate of centroid ¹	0.2605	liver
Ethanol solution concentration [%]	0.0010	liver
Storage time of the sample in Ethanol solution [days]	0.0010	liver
X' — <i>x</i> coordinate of centroid ¹	0.0223	kidneys
Ethanol solution concentration [%]	0.0010	kidneys
Storage time of the sample in Ethanol solution [days]	0.0055	kidneys

¹ Centroid was computed according to the formula available on the link within [20]. In case of a homogenous triangle, the resulting centroid's *x* coordinate is the average of the *x* coordinates of its vertices.

Table 2. Ethanol liver raw data for centroid and Spearman's correlation coefficient computation.

Solution and Soft Tissue	Value X_1 ¹ [-]	Value X_2 ² [-]	Value Y_2 ³ [-]	Value X_3 ⁴ [-]	Value X' ⁵ [-]	Value c ⁶ [%]	Value d ⁷ [Days]
Ethanol, liver	0.2461	0.4303	0.1898	0.4320	0.3695	50	8
Ethanol, liver	0.1200	0.1994	0.1551	0.2004	0.1733	50	17
Ethanol, liver	0.1476	0.223	0.1343	0.2241	0.1982	50	17
Ethanol, liver	0.1329	0.1827	0.1828	0.1838	0.1665	50	17
Ethanol, liver	0.2410	0.3718	0.2465	0.3735	0.3288	100	8
Ethanol, liver	0.1610	0.2374	0.1801	0.2385	0.2123	100	16
Ethanol, liver	0.2771	0.4010	0.4626	0.4028	0.3603	100	8
Ethanol, liver	0.1103	0.1467	0.2147	0.1906	0.1492	100	16
Ethanol, liver	0.2031	0.2048	0.3019	0.2995	0.2358	100	8
Ethanol, liver	0.1153	0.1687	0.2756	0.1704	0.1515	100	16
Ethanol, liver	0.0978	0.0989	0.1842	0.1378	0.1115	100	37

Table 2. *Cont.*

Solution and Soft Tissue	Value X1 ¹ [-]	Value X2 ² [-]	Value Y2 ³ [-]	Value X3 ⁴ [-]	Value X' ⁵ [-]	Value c ⁶ [%]	Value d ⁷ [Days]
Ethanol, liver	0.0836	0.1213	0.1607	0.1519	0.1189	100	37
Ethanol, liver	0.0707	0.1425	0.1233	0.1437	0.1190	100	37

¹ X1—horizontal coordinate of the homogenous triangle (Y1 = 0); ² X2—horizontal coordinate of the homogenous triangle; ³ Y2—vertical coordinate of the homogenous triangle; ⁴ X3—horizontal coordinate of the homogenous triangle (Y3 = 0); ⁵ X'—horizontal coordinate of centroid; ⁶ c—Ethanol solution concentration; ⁷ d—storage time of the sample in Ethanol solution.

Table 3. Ethanol kidney raw data for centroid and Spearman's correlation coefficient computation.

Solution and Soft Tissue	Value X1 ¹ [-]	Value X2 ² [-]	Value Y2 ³ [-]	Value X3 ⁴ [-]	Value X' ⁵ [-]	Value c ⁶ [%]	Value d ⁷ [Days]
Ethanol, kidneys	0.1279	0.1478	0.2493	0.1814	0.1524	50	16
Ethanol, kidneys	0.1170	0.1515	0.1565	0.1532	0.1406	50	7
Ethanol, kidneys	0.1112	0.1753	0.1247	0.1762	0.1542	50	16
Ethanol, kidneys	0.1188	0.1411	0.1385	0.1429	0.1343	100	7
Ethanol, kidneys	0.1055	0.1739	0.1925	0.1747	0.1514	100	16
Ethanol, kidneys	0.1170	0.1463	0.2091	0.1480	0.1371	100	7
Ethanol, kidneys	0.1117	0.2443	0.2452	0.2455	0.2005	100	16
Ethanol, kidneys	0.0669	0.0932	0.0997	0.0939	0.0847	100	7
Ethanol, kidneys	0.1849	0.2733	0.0693	0.2744	0.2442	100	37
Ethanol, kidneys	0.1979	0.2379	0.0568	0.3286	0.2548	100	37
Ethanol, kidneys	0.2002	0.2792	0.1981	0.3239	0.2678	100	37

¹ X1—horizontal coordinate of the homogenous triangle (Y1 = 0); ² X2—horizontal coordinate of the homogenous triangle; ³ Y2—vertical coordinate of the homogenous triangle; ⁴ X3—horizontal coordinate of the homogenous triangle (Y3 = 0); ⁵ X'—horizontal coordinate of centroid; ⁶ c—Ethanol solution concentration; ⁷ d—storage time of the sample in Ethanol solution.

Table 4. Related parameters computed from raw data.

Parameter	Value 7D	Value 8D	Value 16/17D	Value 37D	Note
N day avg centroid x coord.	0.1242	NA	0.1646	0.2556	Ethanol, kidneys
CT number ¹	−379.25	NA	−176.92	277.94	Ethanol, kidneys
N day avg centroid x coord.	NA	0.3236	0.1752	0.1165	Ethanol, liver
CT number ¹	NA	617.92	−124.22	−417.67	Ethanol, liver

¹ CT_number = 5000 × N_dayavg − 1000.

The hypotheses mentioned within the Introduction were evaluated based on these data. This was a test of the alternative hypothesis that the Spearman correlation coefficient is not equal to 0. We used a relationship (see link within the [21]) where, given H0: $r = 0$, the t Student's statistic has a distribution with d.f. (degree of freedom): $N - 2$ (see also link within the [22]).

Ethanol liver: D.f.: 11, p -value: 0.3774 (for ethanol concentration) and D.f.: 11, p -value: 0.0001 (for days stored of the sample in ethanol solution).

Ethanol kidneys: D.f.: 9, p -value: 0.8504 (for ethanol concentration) and D.f.: 9, p -value: 0.00001 (for days stored of the sample in ethanol solution).

Overall, 18 LUTs from 53 LUTs were also validated on selected biological samples, selection of which is illustrated within this section and reported in Figures 9 and 11–13.

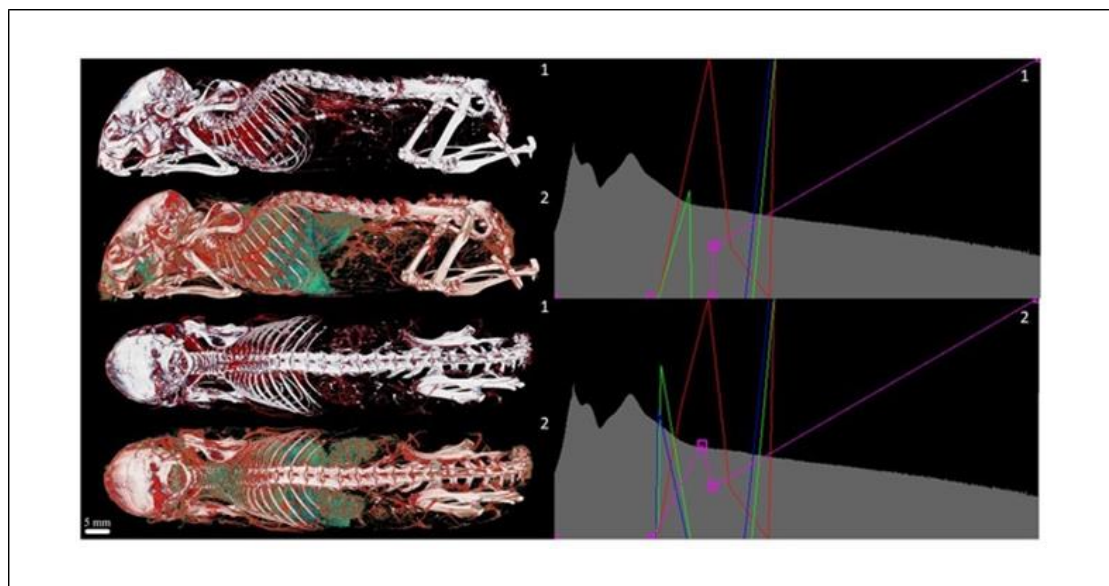


Figure 11. Transfer functions comparison—mouse (Aurovist, 42 kV).

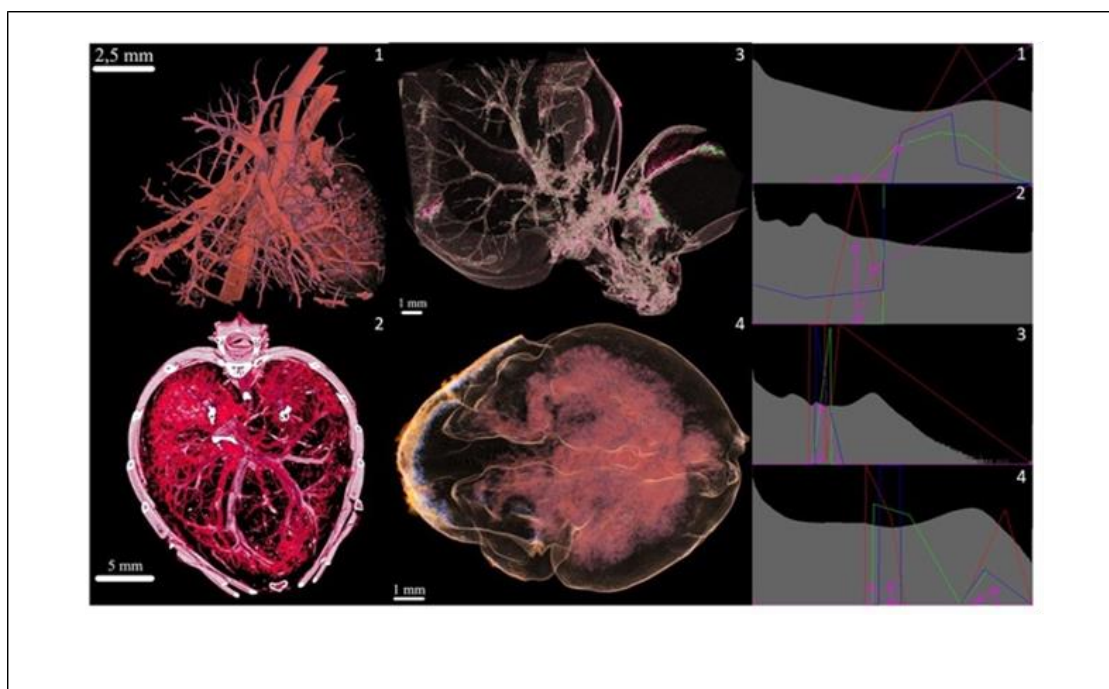


Figure 12. Contrast agents (**left panels**) and relevant transfer functions comparison (**right panels**): 1: Rat lungs and heart (Mercox, 34 kV); 2: Mouse hull (Aurovist, 42 kV); 3: Mouse liver (Omnipaque, 40 kV); and 4: Mouse brain (KI (potassium iodide) + Ethanol, 80 kV).

Due to the large number of results in the form of image data and transfer function, and due to the limited space for publication, only a few ones are presented below. Further significant visualizations, i.e., 18 examples, are available at higher resolution, i.e., with more details according to the contrast agent used, in Appendix A, specifically in Figures A1–A18. Part A1 (Figures A1 and A2) is related to the ethanol contrast, part A2 (Figures A3–A7) to Aurovist, part A3 (Figures A8–A11) to Omnipaque, part A4 (Figures A12–A16) to potassium iodide (KI) in 20% ethanol solution and part A5 (Figures A17 and A18) to Mercor resin. Captions of these figures content detailed descriptions of all possible findings due to the

better contrast visualization. It is the reason why these figures are included with higher spatial resolution within the Appendix A.

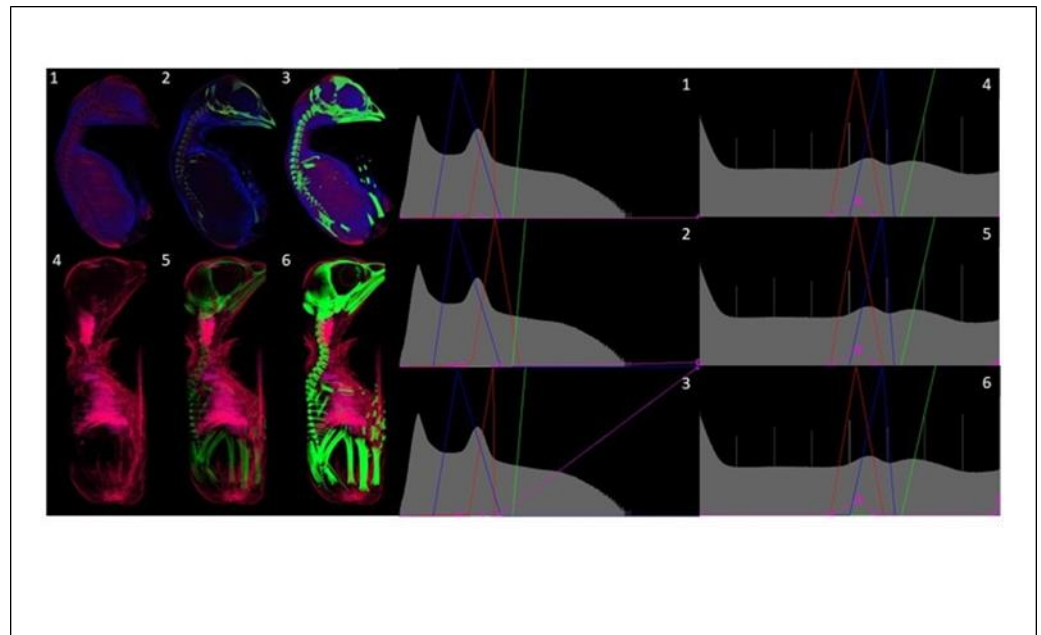


Figure 13. Acquisition voltage comparison in 19 days old chicken. Ethanol, 100 kV (1–3) and 40 kV (4–6).

4. Discussion

The main finding of this study is that there is a statistically significant monotonic relationship between the centroid of the area under the LUT curve and the number of days for which the animal sample was stored in the ethanol solution. H1 of the first hypothesis that the Spearman's correlation coefficient does not equal zero ($r_1 \neq 0$) regarding this relationship was confirmed. On the other hand, there is no statistically significant monotonic relationship between the centroid of the area under the LUT curve and the concentration of the ethanol solution, see Tables 1–4. In this case, H1 of the second hypothesis that the Spearman's correlation coefficient does not equal zero ($r_2 \neq 0$) regarding this relationship was not confirmed. Within Table 4, we can see relevant average values for selected storage days of the specimen and related Hounsfield units, i.e., CT numbers as well. These values are very important and can be assigned to the centroid parameters of a LUT curve incorporating the relevant parameter of days for which the animal sample (mouse liver or kidney) was stored in ethanol solution.

Another finding of the study is that it is not possible to use one universal transfer function for proper soft tissue visualization of μ CT images. The use of an appropriate contrast agent has a very significant effect on soft tissue visualization. It was possible to visualize the capillaries inside the chicken flesh in the phantom vasculature. In the case of the mouse heart, it was possible to segment and colorfully distinguish the tissue of the heart muscle from the rest of the blood vessels.

Due to the lack of one optimal and universal transfer function (LUT), a total of 53 transfer functions were designed using CTvox software [13] and optimized to highlight soft tissues in particular.

In the case of the mouse liver, mainly its external structures can be seen, while in the case of the kidney, brain, and heart, the internal structures are partially visible. In the mouse leg specimen, the transfer function emphasizes partly soft tissue and partly hard tissue (bone).

For the corrosive preparations, the soft tissue structures are shown by the contrast created between the Mercor resin and the air. Since the CT numbers of the synthetic resin

are around 70 HU [2], it is possible to speak of a soft tissue equivalent in this case (range 40–80 HU).

Unfortunately, it was not possible to properly visualize soft tissues or organs from any of the chick scans. In fact, it is not certain that the scan of a stained chicken head of a 19-day-old chick at an anode voltage of 40 kV succeeded in highlighting just the tongue of this chick, or whether it is only the cartilaginous part of its beak.

In *ex vivo* samples of chickens prepared in ethanol and formaldehyde solutions, there was a presumption of contrast in the μ CT images through protein coagulation. This assumption was probably only partially borne out and the result shows the interior of the chicken stained differently in blue and red, corresponding to a slight difference in CT numbers of otherwise further visualizable soft tissue. Furthermore, the ethanol solution in whole chickens did not have the opportunity to penetrate and subsequently evaporate from the animal cavities, which would have caused the solution to be replaced by air, which would have further caused better contrast in the μ CT images (comparable to the evaporation of ethanol from the cavities of the animal organs evaporated therein).

It is also interesting to note that the plastic straw made of polyethylene has approximately the same CT number as the chicken meat and therefore cannot be distinguished from the meat as it passes through it. The glass capillary was the best of all materials to see, as the glass–air interface is a very high contrast object against soft tissue. This was followed by a larger diameter silicone capillary and the third was a smaller diameter capillary. Thus, in contrast to polyethylene, all other materials were clearly distinguishable from chicken meat (Figure 1).

In the majority of cases, the output of CTvox shows that using a lower anode voltage is the optimal choice for scanning soft tissue on μ CT. In the case of bone segmentation, the choice of voltage did not play any significant role. For a more prominent presentation of the results, the processing of the oldest chicks prepared in ethanol was deliberately chosen, mainly because the chick is not sufficiently anatomically developed until around day 19 after egg fertilization, as this is the age at which chicks usually hatch. When younger chicks were examined, many structures were not yet sufficiently developed and, therefore, not visible.

Four chicken samples also contained the contrast agent Aurovist, consisting of 15 nm gold nanoparticles. Specifically, there were two scans at 10 days of age and another two at 12 days of age; unfortunately, no internal (soft) anatomical structures could be identified in this case either. This may have been due to the short age of the chicks, which may not have developed these structures properly yet. A second explanation could be that very low amount of Aurovist contrast agent was injected into the sample.

The limitation of this study is the relatively small number of included images and contrast agents. Another limitation is the use of the purely experimental-based level of visualization, i.e., there is subjective dependence of operator and possible variable deviation. In the case of statistical processing of the data with different KI concentrations, only two different concentrations were used—50% and 100%—this was a limitation, also.

5. Conclusions

In addition to the contrast agents used above, there is possible to use other more suitable contrast agents with very interesting properties. The idea is to perform next study based on the optimal contrast agent selection with relevant LUT. There are prepared comparative experiments with the set of such contrast agents as Sonovue, Iomeron, Optison, Omnipaque, Visipaque, Xenetix, Optiray, and Ultravist to be able to select appropriate one. However, there is assumed utilization of the semi-automatic/automatic LUT setup.

Author Contributions: Conceptualization and methodology, J.M. and J.H.; software, B.G.; validation, J.M. and P.Z.; formal analysis, J.R.; investigation, J.R.; resources, J.M.; data curation, J.M.; writing—original draft preparation, B.G. and J.H.; writing—review and editing, P.Z., G.G., A.L., A.M.; visualization, B.G.; supervision, P.Z.; project administration, J.M.; funding acquisition, J.M. All authors have read and agreed to the published version of the manuscript.

Funding: This research was funded by EU (European Regional Development Fund) and state budget of the Czech Republic, grant number CZ.02.1.01/0.0/0.0/16_019/0000766. The project was supported by Ministry of Education, Youth and Sports of the Czech Republic, Czech Technical University in Prague and Charles University.

Institutional Review Board Statement: The study was approved by the local Ethical Committees of the First and Third Faculty of Medicine, Charles University, Prague, Czech Republic (24185/2019). The animals were treated in accordance with the guidelines defined by the ethical committee, which follows the National Advisory Committee for Laboratory Animal Research (NAC LAR) guidelines. Handling of animals was performed in accordance with the Helsinki Declaration (seventh revision, 2013).

Informed Consent Statement: Not applicable.

Data Availability Statement: The complete original data are not publicly available due to large volume. However, there are available all LUTs as images and *.tf files and relevant images as well. Please, use the link within the [23].

Acknowledgments: There were used uncommercial licenses of software measure CT from Phywe [11,12], CTvox [13] and NRecon [15] from Bruker and Dragonfly [14] from ORS. We would like to thank Phywe, Bruker, and Object Research Systems for their kind support and feedback.

Conflicts of Interest: The authors declare no conflict of interest.

Appendix A

After reconstructing the data with NRecon, we designed several transfer functions in CTvox to emphasize the different structures of the selected samples, especially soft tissues. The CTvox outputs are divided into 5 subsections—according to the method of sample preparation or contrast used. This appendix is an additional section that contains details and data supplemental to the main text above (see the Results section). Figures of replicates for experiments of which representative data are shown in the main text above are added here with higher spatial resolution and detailed description.

Appendix A.1. Ethanol

For the preparations of chickens in ethanol solutions, we have designed transfer characteristics/functions highlighting their structures with different intensities of bone highlighting and then stained the samples with them.

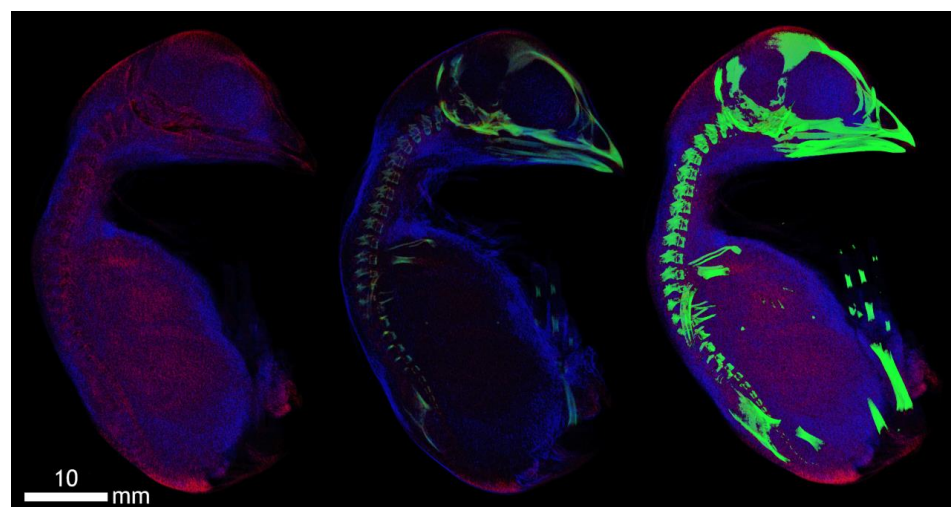


Figure A1. Dyed 19-day-old chicken (acquisition at anode voltage 100 kV, contrast agent ethanol). Ethanol fixed the surface structures of the soft tissues of the skin. The transition of the cartilaginous base of the skeleton (spine, skull, limbs) into bone forms is also shown.

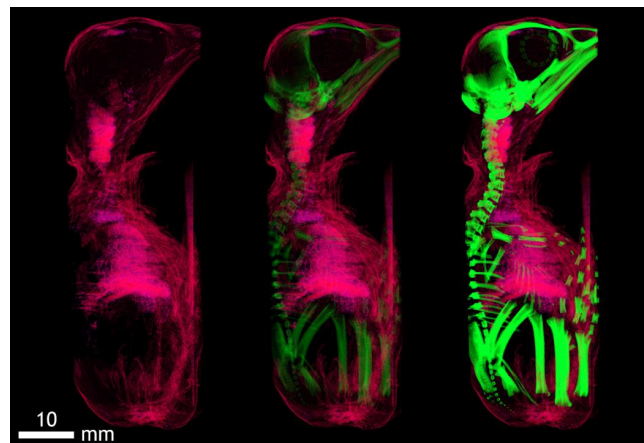


Figure A2. Dyed 19-day-old chicken (acquisition at anode voltage 40 kV, contrast agent ethanol). Imaging after 5 days of ethanol fixation with incipient soft tissue contrast of the trachea, diaphragm, and heart muscle. The contrast in this phase of fixation also corresponds to the density of the surface structures of skin derivatives (feathers).

Appendix A.2. Aurovist

In ex vivo mice with a gold nanoparticles contrast agent (Aurovist), we have designed transfer characteristics/functions that colorfully highlight soft tissue structures, particularly in blood vessels and airways.

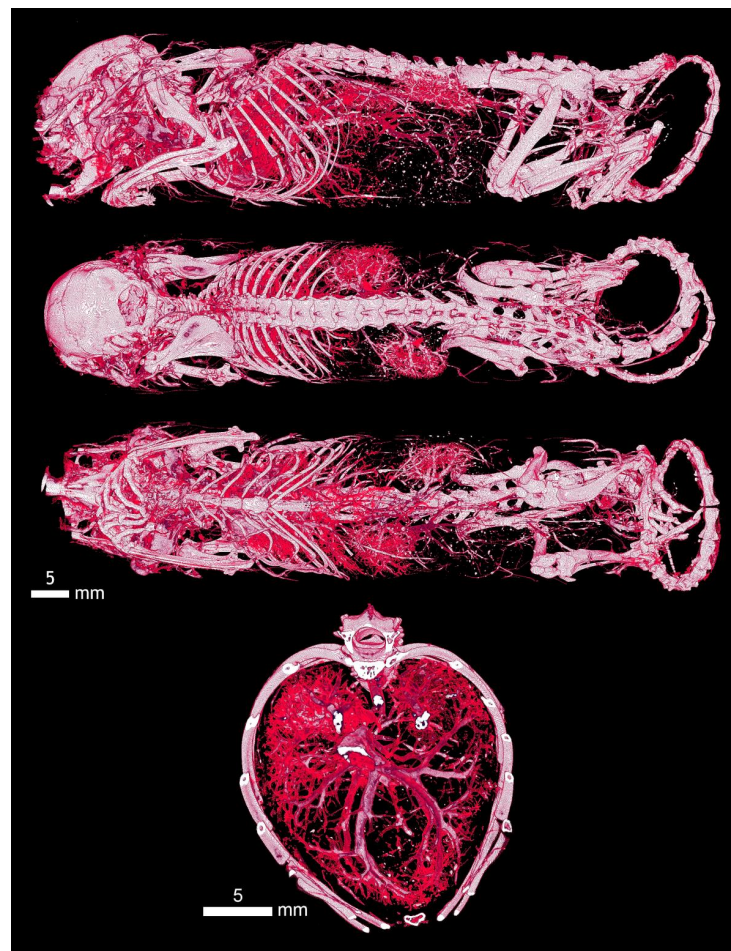


Figure A3. The Aurovist intravascular contrast displayed the entire vascular bed of the mouse. Here, is clearly visible the vasculature of the kidneys and their placement in the retroperitoneum on the

sagittal section, the vessels of the thoracic organs, the hepatic vessels of all lobes, and the supply of the intestines in the abdominal cavity and pelvic plexus. In the section at the level of the thorax, there is a detail of the pulmonary system, where, according to the symmetry of the distribution and branching of the vessels, we can also describe their loss due to occlusion.

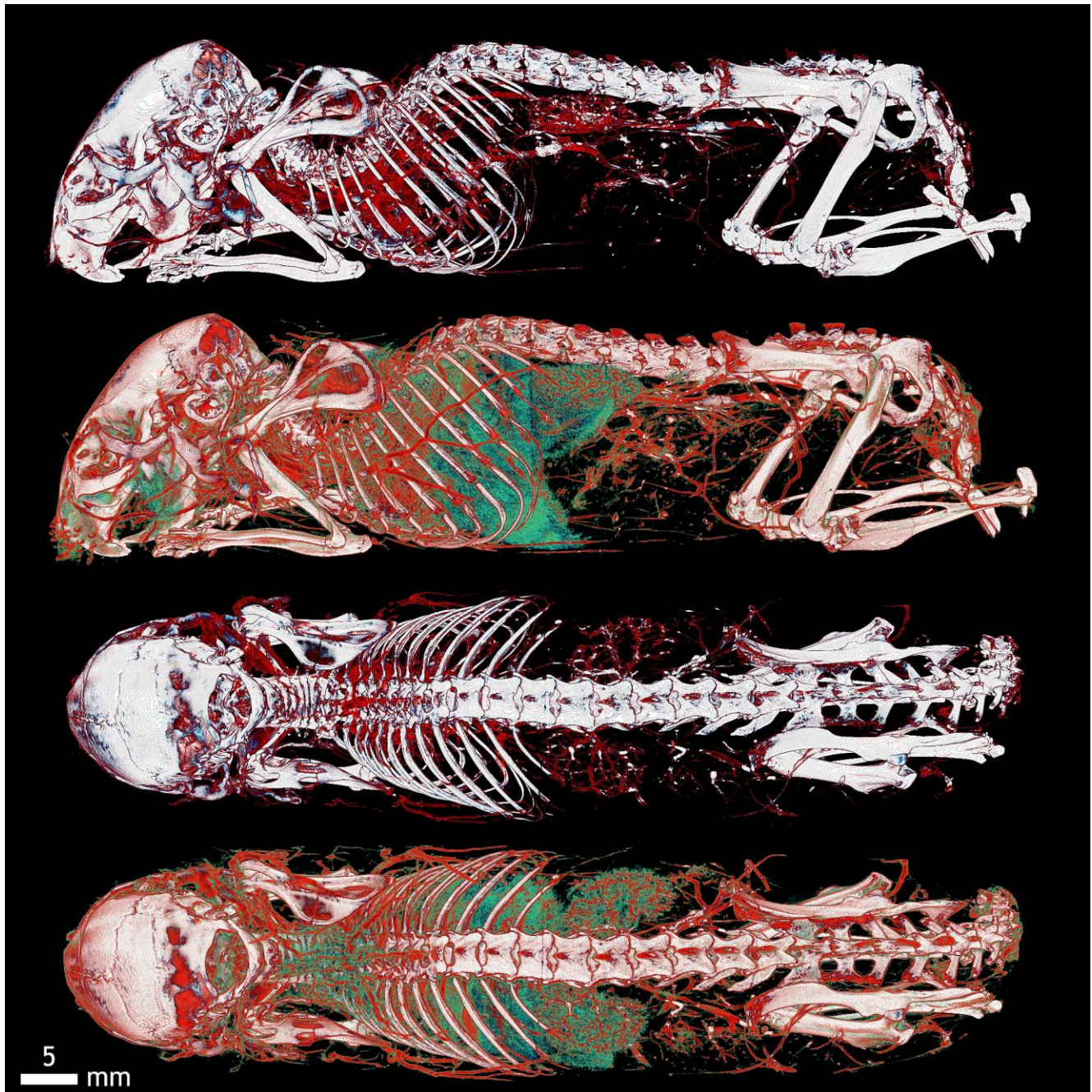


Figure A4. Color resolution of mouse vessels on the body surface (red) and internal organs (green). This distinction also offers a comprehensive view important for the orientation and description of superficial and parietal vessels. In the head area is visible in the external carotid artery branching, then interscapular brown fat vessels, superficial thoracic branching of the thoracic artery and intercostal vessels, parietal lumbar and sacral vessels, as well as plexuses around the spinal canal and limb vessels. The blood vessels of the kidneys and liver here form a network corresponding to the location of the organs in the abdominal cavity, the blood vessels of the heart and lungs to the organs in the chest. This arrangement allows the vessels to be compared at different topographic sites in the body.

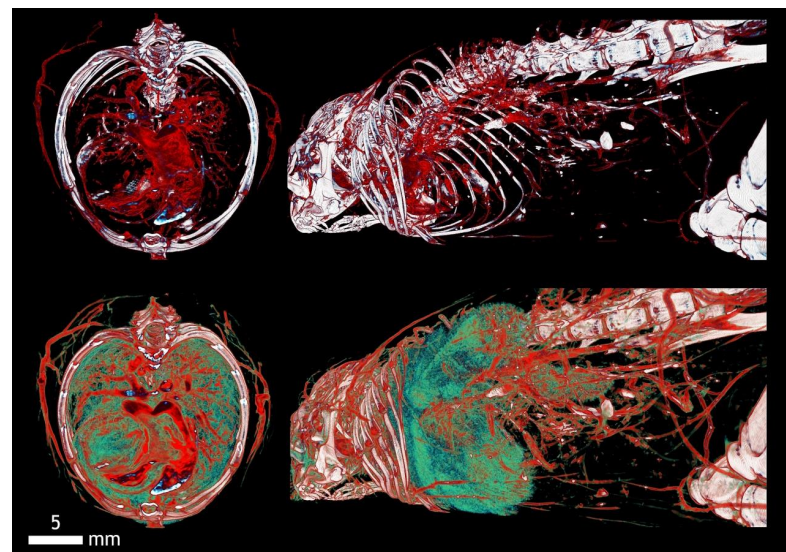


Figure A5. Due to the intravascular contrast of Aurovist, a detailed section of the chest shows the vascular supply of the lungs and its perfusion. Simultaneous view of the bronchial tree allows comparison with respect to the ventilation of individual lung segments. Thus, it is possible to distinguish pathologies in the vascular system in terms of occlusion, embolism, or proliferation in tumor pathology and at the same time monitor the bronchial tree due to air contrast and pathology of reduced aeration in atelectasis and increased air space due to disruption of intrabronchial septum in emphysema.

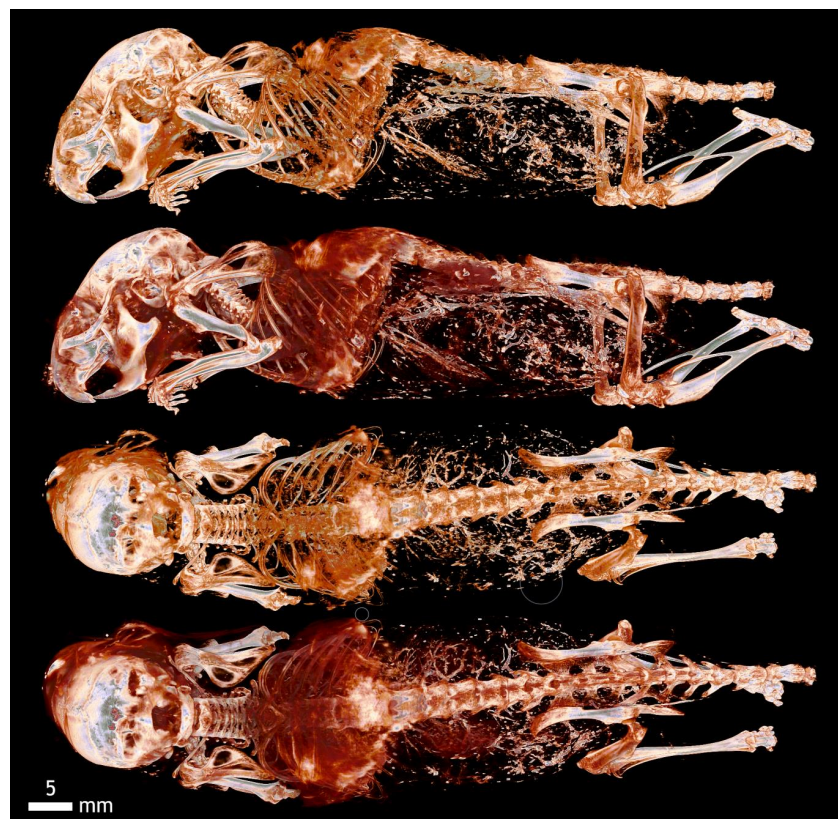


Figure A6. Detail view of the vascular system of the lungs in the chest of the mouse with Aurovist contrast in the sagittal and ventrodorsal scans and detail of the bronchial tree of the lung parenchyma in the same position. It is possible to compare pathologies in the vascular bed and bronchial branching separately.

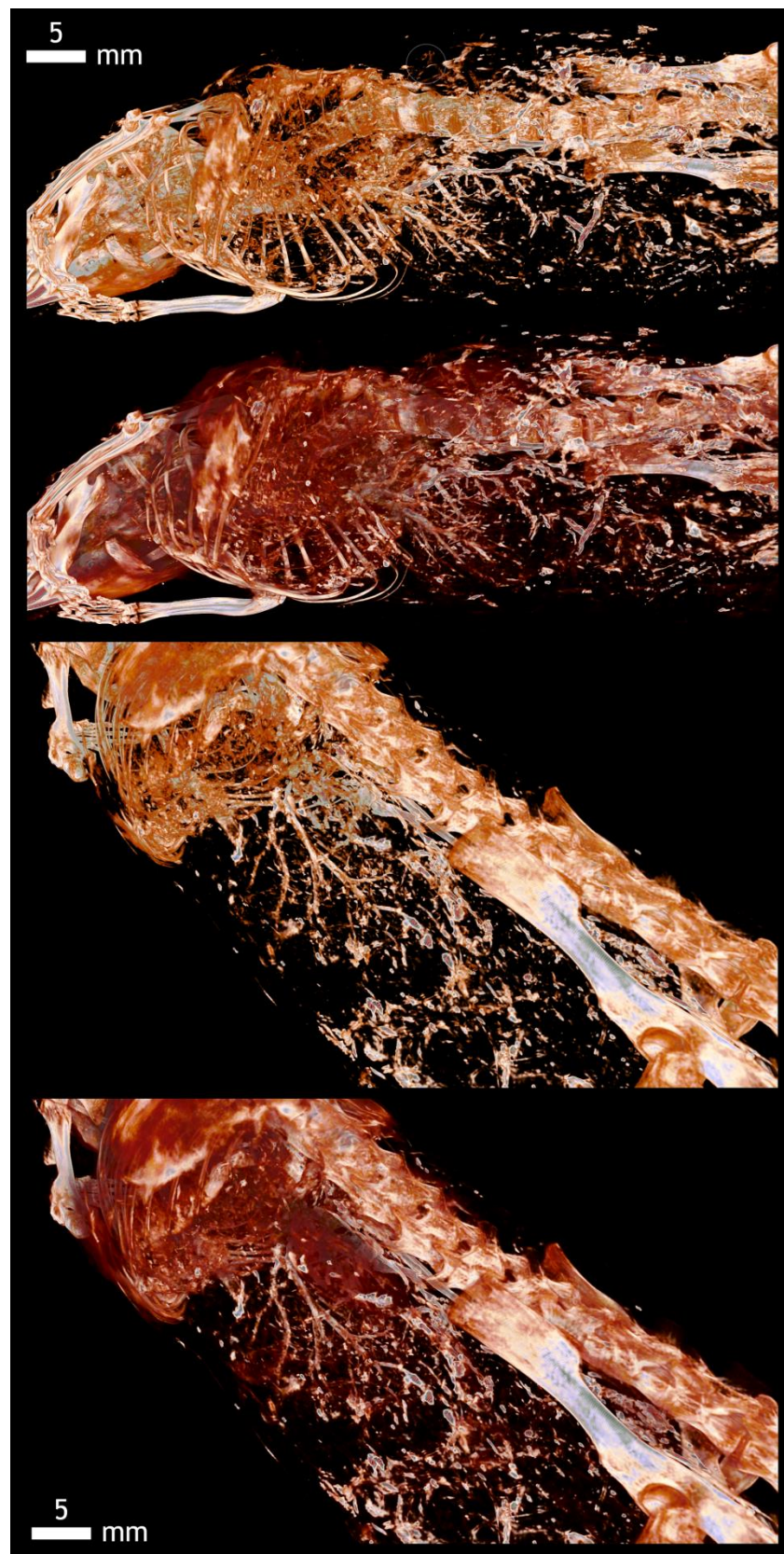


Figure A7. Transition of the thoracic and abdominal cavities and vascular supply of the lungs, heart, and the vessels of the liver and intestine. Simultaneous imaging of the bronchial ventilated tree helps to differentiate individual vascular systems. Detail of the hepatic vessels shows their segmentation into individual lobes. Another vascular system in the abdominal cavity corresponds to the largest perfusion in the bloodstream of the small and large intestine.

Appendix A.3. Omnipaque

In mouse organs prepared with Omnipaque contrast agent, transfer characteristics/functions highlighting the soft tissues of these organs were designed.

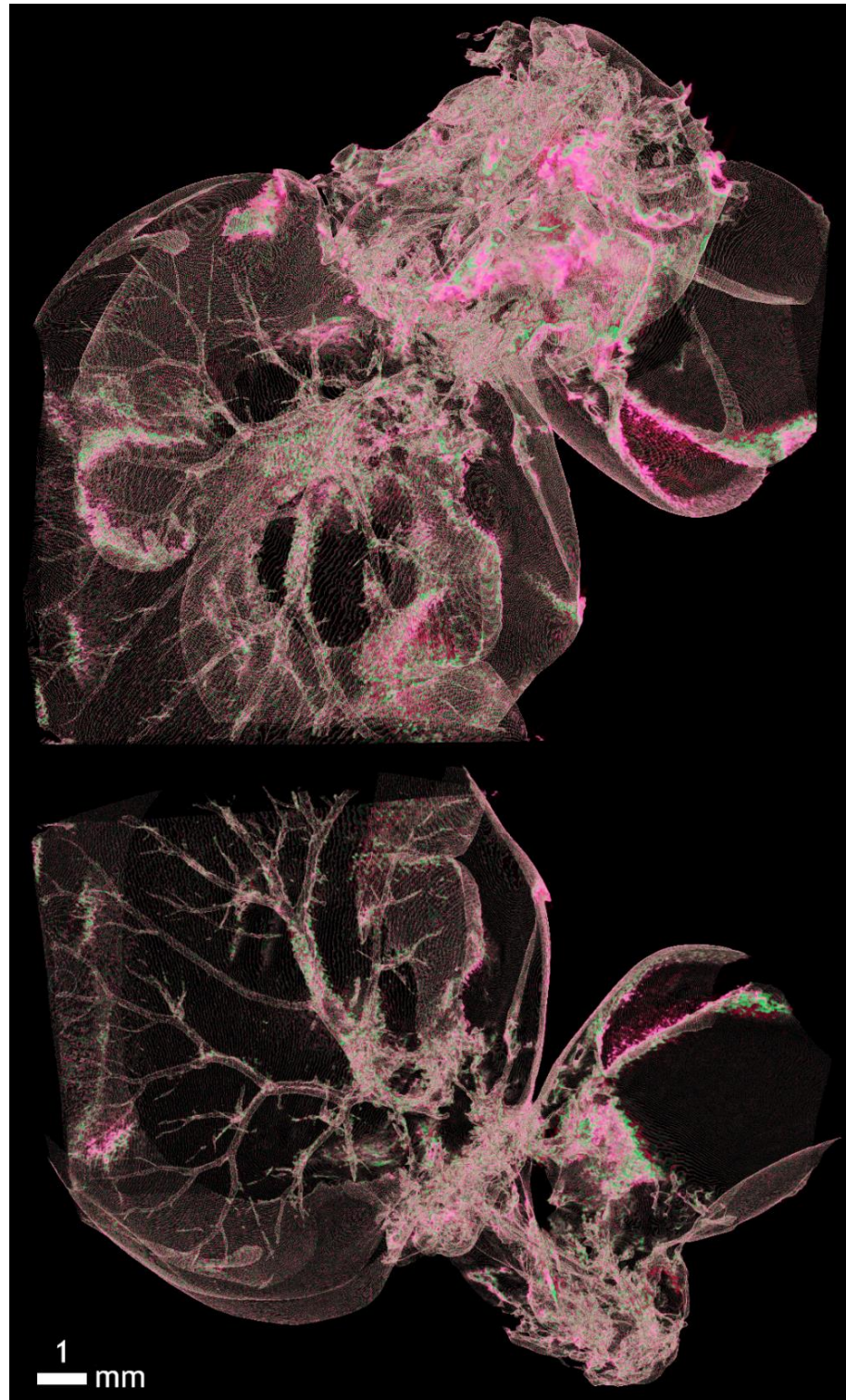


Figure A8. Detailed view of the lobe of the liver and segmental vessels using Omnipaque contrast. Here, is a physiological finding. According to the drawing of the vasculature, we can also describe possible pathological conditions, reconstruction of the liver parenchyma, and its irregular vascular bed or proliferation of blood vessels in tumors.

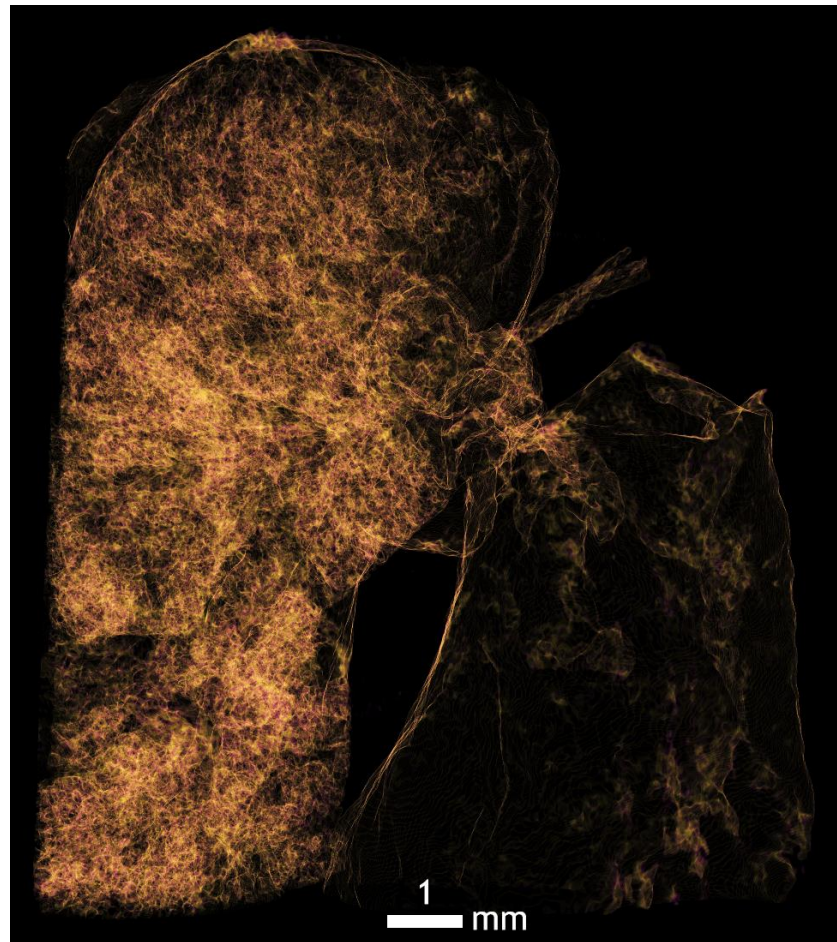


Figure A9. Ideal right lung position for imaging of bronchial branching down to alveolar levels using Omnipaque contrast. The right lung is rotated in a different position and it is possible that post-mortem it collapsed, mechanically vented, or was fixed in the fluid.

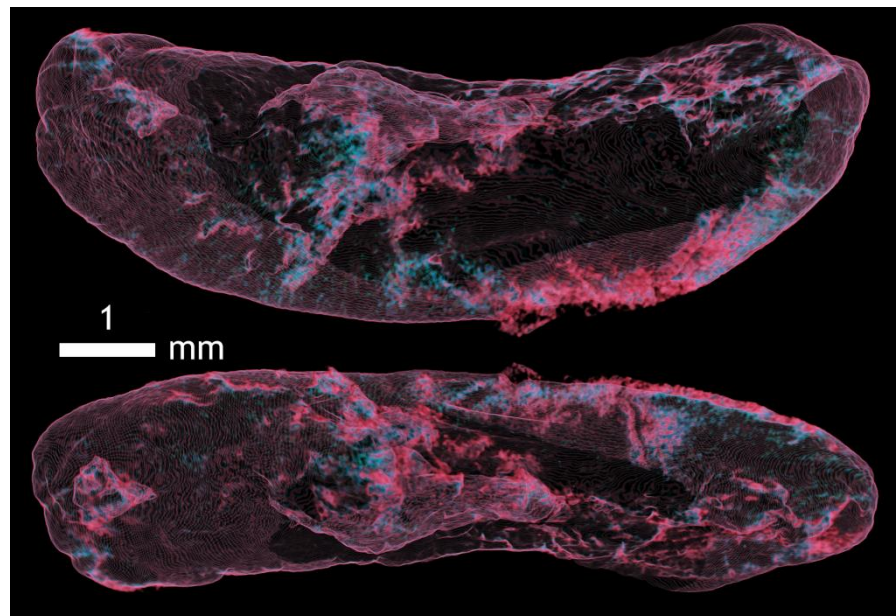


Figure A10. Imaging of the capsule of the spleen and superficial vessels in fascial tissue in two positions using Omnipaque contrast.

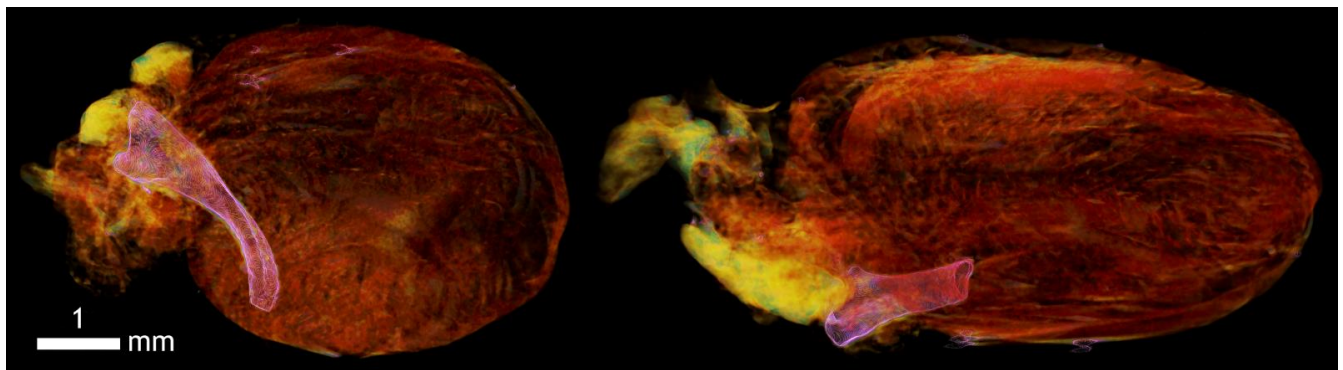


Figure A11. Imaging of superficial vessels of the epicardium and sub fascial layer of the heart.

Appendix A.4. Potassium iodide (KI) in 20% Ethanol Solution

To emphasize soft tissue organs loaded in a solution of dissolved potassium iodide in 20% ethanol solution, additional LUTs were designed and optimized.

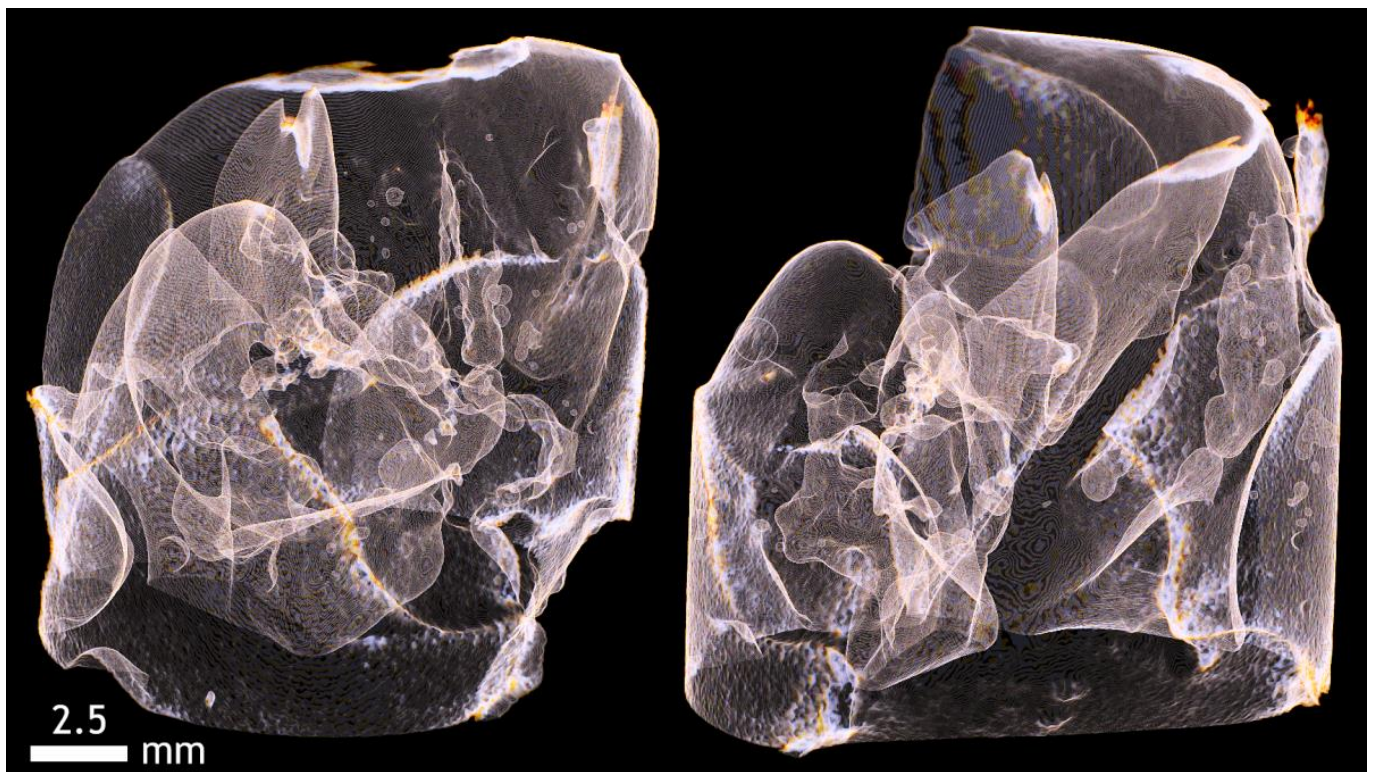


Figure A12. Imaging of the superficial capsule of the liver and division of the hepatic lobes.

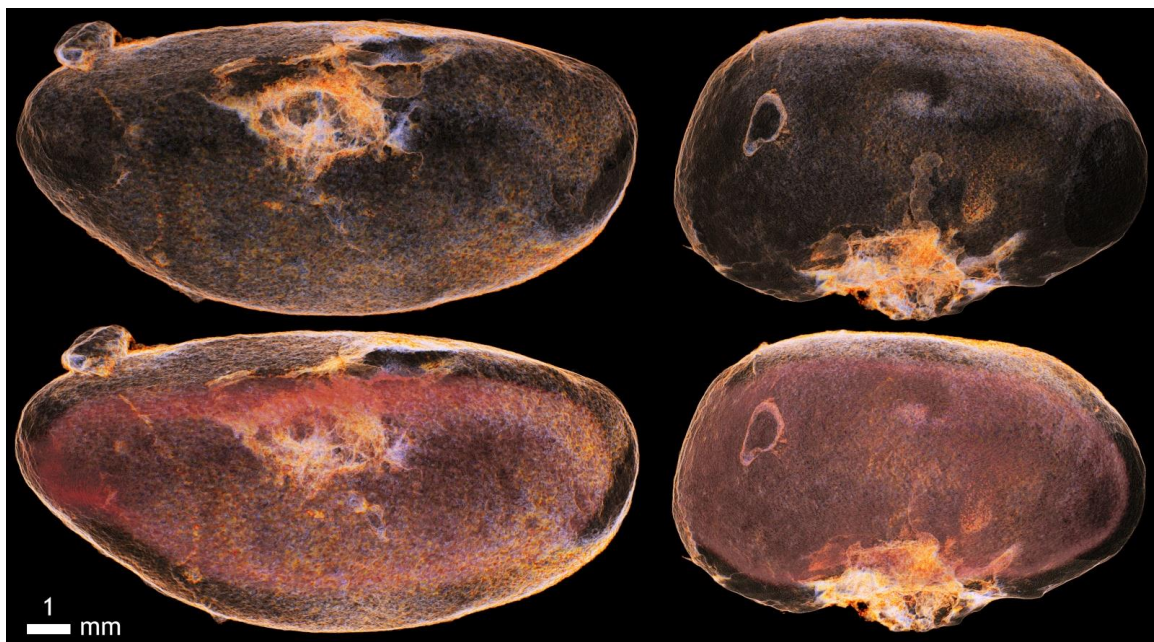


Figure A13. Iodine contrast and imaging of the kidney capsule, including the pathology of the cystic formation on the surface of the kidney.

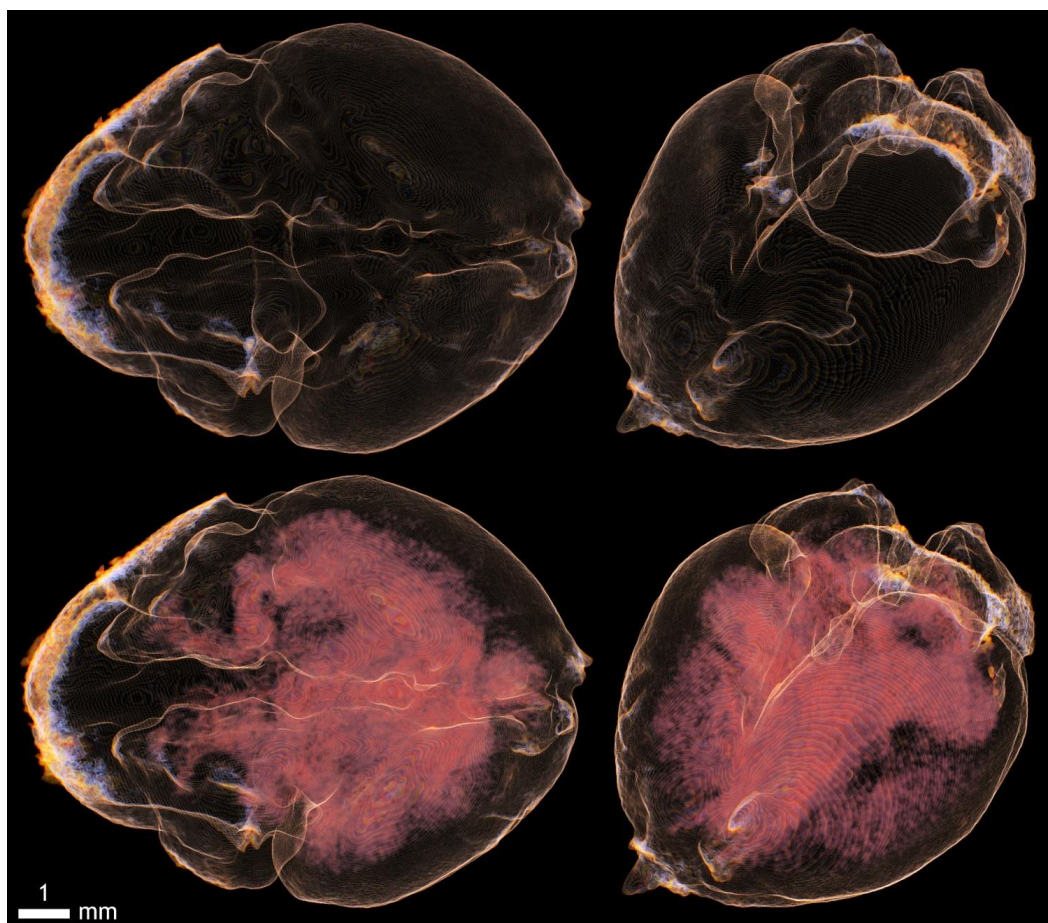


Figure A14. Imaging of the cerebral lobes and internal ventricular system with KI and 20% ethanol.

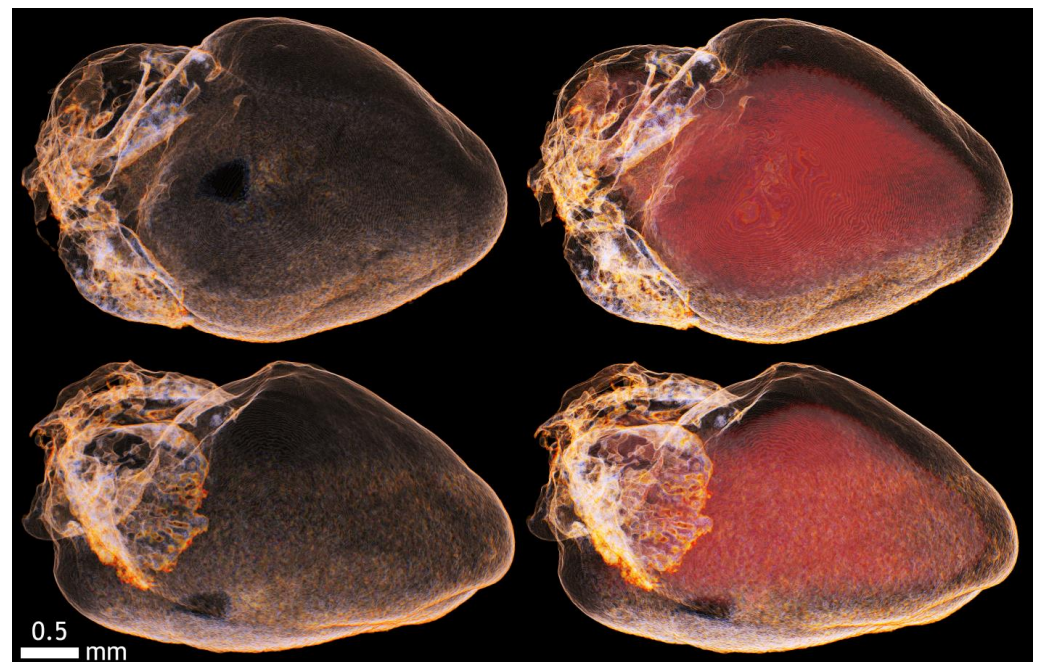


Figure A15. Imaging of the epicardium and endocardium of the heart and its cavities with KI and 20% ethanol.

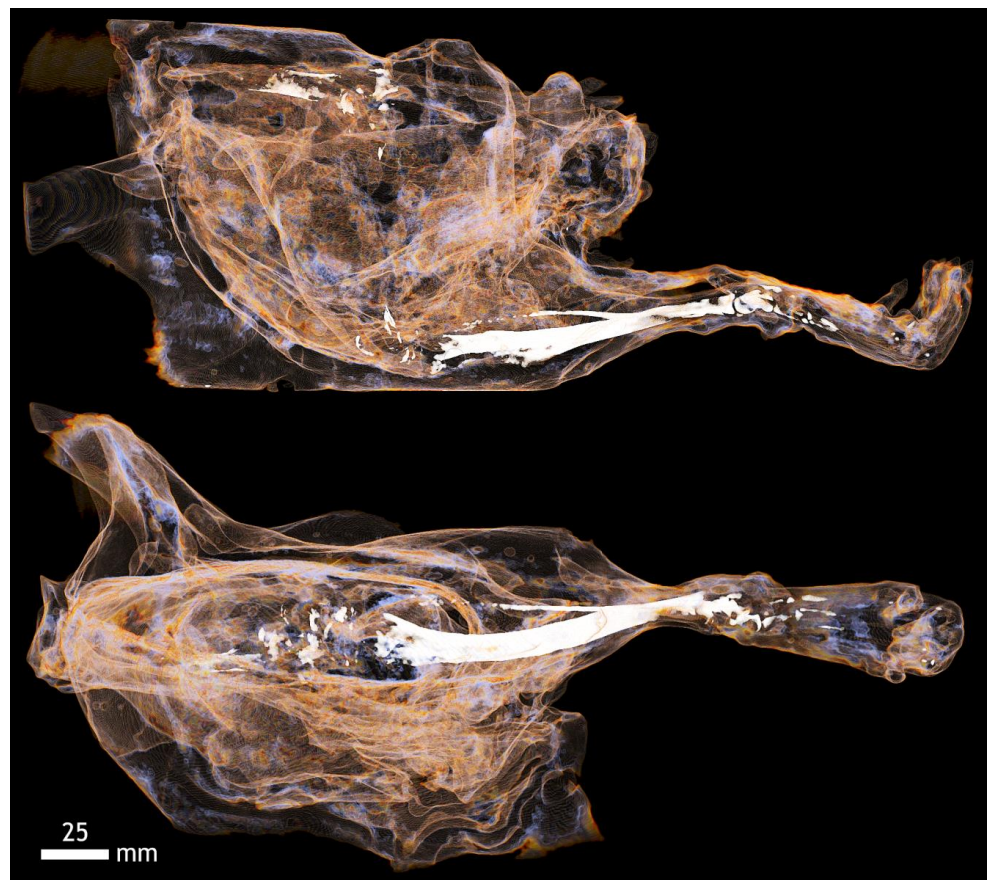


Figure A16. Contrast of fascia muscle groups on the hind limb of mice with KI and 20% ethanol. The bones of the limb can be seen in detail, including the small tarsal bones of the foot.

Appendix A.5. Mercor (Resin)

For corrosive slides, transfer characteristics/functions emphasizing only the soft tissue structures (not the soft tissue itself) have been proposed using a contrast between resin and air. The images show the rabbit and rat airways, and in the case of the rat, the heart is visible along with the vasculature as well.



Figure A17. Rabbit lung vessels visualized by Mercor contrast, a corrosive preparation. Here, the passage of blood vessels in post mortem is ensured by intravenous application of resin by continuous pressure. It is possible to modify vascular ligatures in experiments and, thus, display a failure that is similar to embolism. It is also possible to subsequently measure the angle of the segmental vessels distances and their diameters.

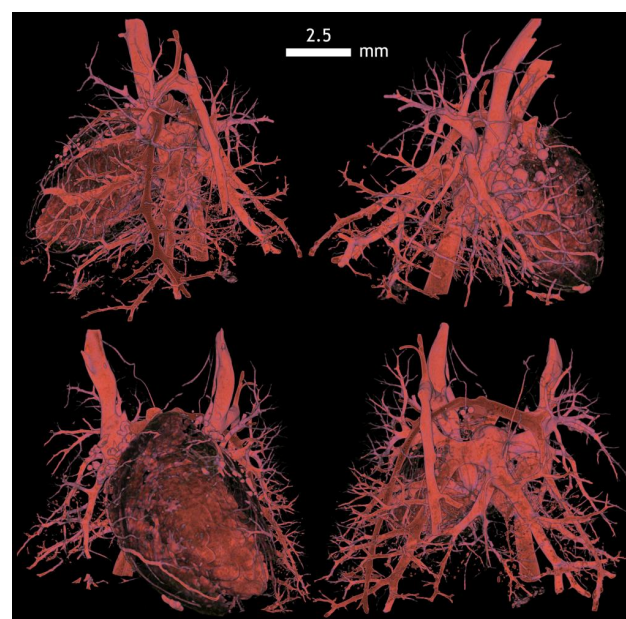


Figure A18. The corrosive specimen of the heart and blood vessels shows both the coronary arteries for the heart, the basic platform for incipient myocardial infarction, and the branching of the pulmonary artery and pulmonary artery diameters and their angles of spacing and segmentation. Here, is a physiological finding. The arrangement of the pulmonary arteries and their branching is disturbed in pulmonary embolism, vascular wall pathology and also in lung tumors.

Appendix B.

This appendix is an additional section that contains details and data supplemental to the main text from the point of view of the experimental setting of both setups, i.e., Phywe and Bruker systems.

Table A1. Values of set parameters on the PHYWE XR 4.0 assembly.

Parameter	Value	Physical Unit
object-source distance	310	mm
detector-source distance	360	mm
anode voltage	35	kV
emission current	1	mA
pixel projection dimension	96	μm
exposure time	500	ms
degree of rotation (incred.)	1.8	
binning ¹	500 × 500	pixels

¹ Explanation of binning is available within the [2,13].

The scan settings for scanning biological samples of chickens outside the shell with the SkyScan 1275 are shown in the following tables. The table header consists of a number followed by a capital letter D, this is the age of the chicken, which is given in days. This may be preceded either by another number followed by the capital letter E, in which case it is the concentration of the ethanol solution in which the chicken was prepared, or by the letter F, which indicates that the chicken was prepared in a formaldehyde solution. In four cases, the concentration of the Ethanol solution is preceded by the capital letter A, this is the contrast agent Aurovist.

Table A2. Values of set parameters on SkyScan 1275.

Parameter	Value 50E5D	Value 100E5D	Value F5D	Value 50E6D	Value 80E6D	Value 100E6D	Physical Unit
object-source distance	40.97	40.97	40.97	40.97	40.97	40.97	mm
detector-source distance	286	286	286	286	286	286	mm
anode voltage	50	50	50	50	50	50	kV
emission current	200	200	200	200	200	200	μA
pixel projection dimension	11.6	11.6	11.6	11.6	11.6	11.6	μm
exposure time	50	50	50	50	50	50	ms
degree of rotation (incred.)	0.2	0.2	0.2	0.2	0.2	0.2	
binning ¹	1 × 1	1 × 1	1 × 1	1 × 1	1 × 1	1 × 1	pixel

¹ Explanation of binning is available within the [2,13].

Table A3. Values of set parameters on SkyScan 1275.

Parameter	Value F6D	Value 80E7D	Value 100E7D	Value 80E8D	Value 80E9D	Value A80E10D	Physical Unit
object-source distance	40.97	48.39	48.39	57.22	71.47	92.67	mm
detector-source distance	286	286	286	286	286	286	mm
anode voltage	50	50	50	65	70	100	kV
emission current	200	200	200	153	142	100	μA
pixel projection dimension	11.6	13.7	13.7	16.2	20.24	26.24	μm
exposure time	50	50	50	36	36	35	ms
degree of rotation (incred.)	0.2	0.2	0.2	0.2	0.2	0.2	°
binning ¹	1 × 1	1 × 1	1 × 1	1 × 1	1 × 1	1 × 1	pixel

¹ Explanation of binning is available within the [2,13].

Table A4. Values of set parameters on SkyScan 1275.

Parameter	Value A80E10D	Value 80E10-11D	Value 80E10-11D	Value 50E11D	Value 80E12D	Physical Unit
object-source distance	71.47	60.75	67.9	92.67	80.4	mm
detector-source distance	286	286	286	286	286	mm
anode voltage	75	75	75	75	75	kV
emission current	133	133	133	133	133	μA
pixel projection dimension	20.24	17.2	19.23	26.24	22.77	μm
exposure time	36	36	36	36	500	ms
degree of rotation (incrm.)	0.2	0.2	0.2	0.2	0.2	°
binning ¹	1 × 1	1 × 1	1 × 1	1 × 1	1 × 1	pixel

¹ Explanation of binning is available within the [2,13].**Table A5.** Values of set parameters on SkyScan 1275.

Parameter	Value A80E12D	Value A80E12D	Value 50E13D	Value 50E14D	Value 100E14D	Physical Unit
object-source distance	92.67	82.19	92.67	96.48	123.29	mm
detector-source distance	286	286	286	286	286	mm
anode voltage	75	75	75	75	80	kV
emission current	133	133	133	133	125	μA
pixel projection dimension	26.24	23.27	26.24	27.32	34.91	μm
exposure time	500	500	500	500	32	ms
degree of rotation (incrm.)	0.2	0.2	0.2	0.2	0.2	°
binning ¹	1 × 1	1 × 1	1 × 1	1 × 1	1 × 1	pixel

¹ Explanation of binning is available within the [2,13].**Table A6.** Values of set parameters on SkyScan 1275.

Parameter	Value 50E15D	Value 50E15D	Value 50E16D	Value 100E18D	Value 100E18D	Physical Unit
object-source distance	146.51	142.94	178.67	169.74	176.89	mm
detector-source distance	286	286	286	286	286	mm
anode voltage	80	80	80	80	80	kV
emission current	125	125	125	125	125	μA
pixel projection dimension	41.48	40.47	50.59	48.06	50.08	μm
exposure time	32	32	32	33	33	ms
degree of rotation (incrm.)	0.2	0.2	0.2	0.2	0.2	°
binning ¹	1 × 1	1 × 1	1 × 1	1 × 1	1 × 1	pixel

¹ Explanation of binning is available within the [2,13].**Table A7.** Values of set parameters on SkyScan 1275.

Parameter	Value 100E19D	Value 100E19D	Value 100E19D	Value 100E19D	Physical Unit
object-source distance	173.31	132.22	92.67	141.15	mm
detector-source distance	287	286	286	286	mm
anode voltage	40	80	100	100	kV
emission current	250	125	100	100	μA
pixel projection dimension	49.07	37.44	26.24	39.97	μm
exposure time	35	35	35	35	ms
degree of rotation (incrm.)	0.2	0.2	0.2	0.2	°
binning ¹	1 × 1	1 × 1	1 × 1	1 × 1	pixel

¹ Explanation of binning is available within the [2,13].

The scanning parameters for scanning biological samples of chickens in the shell with the SkyScan 1275 are shown in the following tables. The table header consists of a number followed by a capital letter D, this is the age of the chicken, which is given in days.

Table A8. Values of set parameters on SkyScan 1275.

Parameter	Value 8D	Value 9D	Value 10D	Value 11D	Value 12D	Physical Unit
object-source distance	155.45	146.51	151.87	137.58	153.66	mm
detector-source distance	286	286	286	286	286	mm
anode voltage	80	80	80	80	80	kV
emission current	125	125	125	125	125	μA
pixel projection dimension	44.01	41.48	43	38.95	43.51	μm
exposure time	36	36	36	36	36	ms
degree of rotation (incrim.)	0.2	0.2	0.2	0.2	0.2	
binning ¹	1 × 1	1 × 1	1 × 1	1 × 1	1 × 1	pixel

¹ Explanation of binning is available within the [2,13].

Table A9. Values of set parameters on SkyScan 1275.

Parameter	Value 13D	Value 14D	Value 15D	Value 15D	Value 16D	Physical Unit
object-source distance	146.51	148.30	155.45	158.93	144.73	mm
detector-source distance	286	286	286	286	286	mm
anode voltage	80	80	80	80	80	kV
emission current	125	125	125	125	125	μA
pixel projection dimension	41.48	41.49	44.01	45	40.98	μm
exposure time	36	36	36	36	36	ms
degree of rotation (incrim.)	0.2	0.2	0.2	0.2	0.2	
binning ¹	1 × 1	1 × 1	1 × 1	1 × 1	1 × 1	pixel

¹ Explanation of binning is available within the [2,13].

Table A10. Values of set parameters on SkyScan 1275.

Parameter	Value 17D	Value 18D	Value 18D	Value 19D	Physical Unit
object-source distance	159.02	157.23	167.95	150.09	mm
detector-source distance	286	286	286	286	mm
anode voltage	95	80	80	80	kV
emission current	105	125	125	125	μA
pixel projection dimension	45.03	44.52	47.55	42.50	μm
exposure time	36	36	36	36	ms
degree of rotation (incrim.)	0.2	0.2	0.2	0.2	
binning ¹	1 × 1	1 × 1	1 × 1	1 × 1	pixel

¹ Explanation of binning is available within the [2,13].

Table A11. Values of set parameters on SkyScan 1275 for scanning of the 13 liver samples.

Parameter	Value 50E8D	Value 50E17D	Value 100E8D	Value 100E16D	Value 100E37D	Physical Unit
object-source distance	63.57	56.51	54.74	52.98	49.45	mm
detector-source distance	286	286	286	286	286	mm
anode voltage	30	40	30	35	40	kV
emission current	212	250	212	231	250	μA
pixel projection dimension	18.00	16.00	15.50	15.00	14.00	μm
exposure time	58	35	58	38	35	ms
degree of rotation (incred.)	0.2	0.2	0.2	0.2	0.2	
binning ¹	1 × 1	1 × 1	1 × 1	1 × 1	1 × 1	pixel

¹ Explanation of binning is available within the [2,13].**Table A12.** Values of set parameters on SkyScan 1275 for scanning of the 11 kidneys samples.

Parameter	Value 50E7D	Value 50E16D	Value 100E7D	Value 100E16D	Value 100E37D	Physical Unit
object-source distance	28.26	28.26	30.02	28.26	28.26	mm
detector-source distance	286	286	286	286	286	mm
anode voltage	35	35	35	35	40	kV
emission current	231	231	231	231	250	μA
pixel projection dimension	8.00	8.00	8.50	8.00	8.00	μm
exposure time	35	38	35	38	35	ms
degree of rotation (incred.)	0.2	0.2	0.2	0.2	0.2	
binning ¹	1 × 1	1 × 1	1 × 1	1 × 1	1 × 1	pixel

¹ Explanation of binning is available within the [2,13].**Table A13.** Values of set parameters on SkyScan 1275.

Parameter	Value 17D	Value 18D	Value 18D	Value 19D	Physical Unit
object-source distance	159.02	157.23	167.95	150.09	mm
detector-source distance	286	286	286	286	mm
anode voltage	95	80	80	80	kV
emission current	105	125	125	125	μA
pixel projection dimension	45.03	44.52	47.55	42.50	μm
exposure time	36	36	36	36	ms
degree of rotation (incred.)	0.2	0.2	0.2	0.2	
binning ¹	1 × 1	1 × 1	1 × 1	1 × 1	pixel

¹ Explanation of binning is available within the [2,13].**Table A14.** Values of set parameters on SkyScan 1275.

Parameter	Value 17D	Value 18D	Value 18D	Value 19D	Physical Unit
object-source distance	159.02	157.23	167.95	150.09	mm
detector-source distance	286	286	286	286	mm
anode voltage	95	80	80	80	kV
emission current	105	125	125	125	μA
pixel projection dimension	45.03	44.52	47.55	42.50	μm
exposure time	36	36	36	36	ms
degree of rotation (incred.)	0.2	0.2	0.2	0.2	°
binning ¹	1 × 1	1 × 1	1 × 1	1 × 1	pixel

¹ Explanation of binning is available within the [2,13].

Table A15. Values of set parameters on SkyScan 1275.

Parameter	Value 17D	Value 18D	Value 18D	Value 19D	Physical Unit
object-source distance	159.02	157.23	167.95	150.09	mm
detector-source distance	286	286	286	286	mm
anode voltage	95	80	80	80	kV
emission current	105	125	125	125	μA
pixel projection dimension	45.03	44.52	47.55	42.50	μm
exposure time	36	36	36	36	ms
degree of rotation (incrim.)	0.2	0.2	0.2	0.2	°
binning ¹	1 × 1	1 × 1	1 × 1	1 × 1	pixel

¹ Explanation of binning is available within the [2,13].**Table A16.** Values of set parameters on SkyScan 1275.

Parameter	Value 17D	Value 18D	Value 18D	Value 19D	Physical Unit
object-source distance	159.02	157.23	167.95	150.09	mm
detector-source distance	286	286	286	286	mm
anode voltage	95	80	80	80	kV
emission current	105	125	125	125	μA
pixel projection dimension	45.03	44.52	47.55	42.50	μm
exposure time	36	36	36	36	ms
degree of rotation (incrim.)	0.2	0.2	0.2	0.2	°
binning ¹	1 × 1	1 × 1	1 × 1	1 × 1	pixel

¹ Explanation of binning is available within the [2,13].

The scan settings for scanning mouse biological samples with Aurovist contrast agent (letter A), rabbit and rat biological samples with Mercor resin contrast agent (letter M), and mouse organ biological samples with Omnipaque contrast agent (letter O) and potassium iodide (KI) contrast agent dissolved in 20% ethanol solution (letters KI) with the SkyScan 1275 kit are shown in the following tables.

Table A17. Values of set parameters on SkyScan 1275.

Parameter	Value A-Mouse	Value M-Rabbit	Value M-Rat	Physical Unit
object-source distance	92.67	148.30	62.54	mm
detector-source distance	286	286	286	mm
anode voltage	42	46	34	kV
emission current	238	217	227	μA
pixel projection dimension	26.24	41.99	17.71	μm
exposure time	99	35	41	ms
degree of rotation (incrim.)	0.2	0.2	0.2	°
binning ¹	1 × 1	1 × 1	1 × 1	pixel

¹ Explanation of binning is available within the [2,13].

Table A18. Values of set parameters on SkyScan 1275.

Parameter	Value O-Liver	Value O-Lungs	Value O-Spleen	Value O-Heart	Physical Unit
object-source distance	58.96	33.95	28.59	33.95	mm
detector-source distance	286	286	286	286	mm
anode voltage	40	54	54	40	kV
emission current	238	185	185	238	μA
pixel projection dimension	16.70	19.22	16.19	9.61	μm
exposure time	35	50	50	35	ms
degree of rotation (incrim.)	0.2	0.4	0.4	0.2	
binning ¹	1 × 1	2 × 2	2 × 2	1 × 1	pixels

¹ Explanation of binning is available within the [2,13].**Table A19.** Values of set parameters on SkyScan 1275.

Parameter	Value KI-Liver	Value KI-Kidney	Value KI-Brain	Value KI-Heart	Value KI-Leg	Physical Unit
object-source distance	107.21	32.16	117.93	39.31	178.67	mm
detector-source distance	286	286	286	286	286	mm
anode voltage	80	80	80	80	80	kV
emission current	125	125	125	125	125	μA
pixel projection dimension	30.36	9.11	33.39	11.13	50.59	μm
exposure time	35	35	35	35	35	ms
degree of rotation (incrim.)	0.2	0.2	0.2	0.2	0.2	
binning ¹	1 × 1	1 × 1	1 × 1	1 × 1	1 × 1	pixel

¹ Explanation of binning is available within the [2,13].

References

- Liguori, C.; Frauenfelder, G.; Massaroni, C.; Saccomandi, P.; Giurazza, F.; Pitocco, F.; Marano, R.; Schena, E. Emerging clinical applications of computed tomography. *Med. Devices* **2015**, *8*, 265–278. [\[CrossRef\]](#)
- Stock, S.R. *Microcomputed Tomography: Methodology and Applications*, 2nd ed.; CRC Press/Taylor and Francis: Boca Raton, FL, USA, 2020.
- Vickerton, P.; Jarvis, J.; Jeffery, N. Concentration-dependent specimen shrinkage in iodine-enhanced microCT. *J. Anat.* **2013**, *223*, 185–193. [\[CrossRef\]](#) [\[PubMed\]](#)
- Silva, J.M.D.E.; Zanette, I.; Noel, P.B.; Cardoso, M.B.; Kimm, M.A.; Pfeiffer, F. Three-dimensional non-destructive soft-tissue visualization with X-ray staining micro-tomography. *Sci. Rep.* **2015**, *5*, 14088. [\[CrossRef\]](#) [\[PubMed\]](#)
- Metscher, B.D. MicroCT for comparative morphology: Simple staining methods allow high-contrast 3D imaging of diverse non-mineralized animal tissues. *BMC Physiol.* **2009**, *9*, 11. [\[CrossRef\]](#) [\[PubMed\]](#)
- Patzelt, M.; Mrzilkova, J.; Dudak, J.; Krejci, F.; Zemlicka, J.; Karch, J.; Musil, V.; Rosina, J.; Sykora, V.; Horehledova, B.; et al. Ethanol fixation method for heart and lung imaging in micro-CT. *Jpn. J. Radiol.* **2019**, *37*, 500–510. [\[CrossRef\]](#) [\[PubMed\]](#)
- Dudak, J.; Zemlicka, J.; Karch, J.; Patzelt, M.; Mrzilkova, J.; Zach, P.; Hermanova, Z.; Kvacek, J.; Krejci, F. High-contrast X-ray micro-radiography and micro-CT of ex-vivo soft tissue murine organs utilizing ethanol fixation and large area photon-counting detector. *Sci. Rep.* **2016**, *6*, 30385. [\[CrossRef\]](#) [\[PubMed\]](#)
- McNitt-Gray, M.F.; Taira, R.K.; Johnson, S.L.; Razavi, M. An automatic method for enhancing the display of different tissue densities in digital chest radiographs. *J. Digit. Imaging* **1993**, *6*, 95–104. [\[CrossRef\]](#) [\[PubMed\]](#)
- Seeram, E.; Seeram, D. Image Postprocessing in Digital Radiology—A Primer for Technologists. *J. Med. Imaging Radiat. Sci.* **2008**, *39*, 23–41. [\[CrossRef\]](#) [\[PubMed\]](#)
- Alshipli, M.; Kabir, N.A.; Hashim, R.; Marashdeh, M.W.; Tajuddin, A.A. Measurement of attenuation coefficients and CT numbers of epoxy resin and epoxy-based Rhizophora spp. particleboards in computed tomography energy range. *Radiat. Phys. Chem.* **2018**, *149*, 41–48. [\[CrossRef\]](#)
- Phywe XR 4.0 Expert Unit, X-ray Unit, 35 kV: Germany: PHYWE Systeme GmbH. Available online: <https://repository.curriculab.net/files/bedanl.pdf/09057.99/0905799e.pdf> (accessed on 18 July 2021).
- XR 4.0 Software Measure CT Manual. PHYWE. Available online: <https://repository.curriculab.net/files/bedanl.pdf/14421.61/1442161e.pdf> (accessed on 18 July 2021).
- CTvox Quick Start Guide. Bruker. Available online: https://www.bruker.com/fileadmin/user_upload/3-Service/Support/Preclinical_Imaging/X-Ray-uCT_Software/CTvox_QuickStartGuide.pdf (accessed on 18 July 2021).
- Key Features of Dragonfly. Available online: <https://www.theobjects.com/dragonfly/features.html> (accessed on 18 July 2021).

15. NRecon User Manual. Available online: https://umanitoba.ca/faculties/health_sciences/medicine/units/cacs/sam/media/NReconUserManual.pdf (accessed on 18 July 2021).
16. MIPS (Medical/Microscopy Image Processing Software). Available online: <http://webzam.fbmi.cvut.cz/hozman/> (accessed on 20 February 2022).
17. DICOM PS3.3 2021e—Information Object Definitions. C.11 LUT and Presentation States. Available online: https://dicom.nema.org/medical/dicom/current/output/chtml/part03/sect_C.11.2.htm (accessed on 28 November 2021).
18. Weiss, S.; Westermann, R. Differentiable Direct Volume Rendering. *IEEE Trans. Vis. Comput. Graph.* **2022**, *28*, 562–572. [CrossRef] [PubMed]
19. Skyscan CT-Volume Manual. Available online: https://umanitoba.ca/faculties/health_sciences/medicine/units/cacs/sam/media/CTVol_UserManual.pdf (accessed on 18 July 2021).
20. Wolfram Research, Inc. Centroid of triangle—Wolfram Alpha. Wolfram Research, Inc., Champaign, IL. Available online: <https://www.wolframalpha.com/input?i=centroid+of+triangle> (accessed on 6 April 2022).
21. Stakat. Let's Master Statistics Together. Spearman's Rho. Available online: <https://statkat.com/stat-tests/spearmans-rho.php#5> (accessed on 25 April 2022).
22. Real Statistics Using Excel. Spearman's Rank Correlation Hypothesis Testing. Available online: <https://www.real-statistics.com/correlation/spearmans-rank-correlation/spearmans-rank-correlation-detailed/> (accessed on 25 April 2022).
23. Gaspar, B.; Mrzilkova, J.; Hozman, J.; Zach, P.; Lahutsina, A.; Morozova, A.; Guarnieri, G.; Riedlova, J. Data Availability Statement: There Are Available All LUTs as Images and *.tf Files and Relevant Images as Well. Available online: <http://webzam.fbmi.cvut.cz/hozman/LUT.htm> (accessed on 25 April 2022).